Journal of The
Electrochemical Society

OPEN ACCESS

Deconvolution of an SoC- and SoH-Dependent Contact Resistance in a Multilayer Pouch Cell Using Impedance Spectroscopy

To cite this article: Simon Helmer *et al* 2026 *J. Electrochem. Soc.* **173** 010504

View the article online for updates and enhancements.

You may also like

- Theoretical Insights into Equilibrium Potentials in Electrochemical Cells with Multiple Mobile Charge Carriers
Felix Ehrlich, Akhil Ashar, Oscar Furst et al.
- Electrolyte Motion–Induced Salt Inhomogeneity (EMSI) Can Occur Across Cell Formats: A Mechanistic Study in Single-layer Pouch Cells and Mitigation Strategies
Hao-Chen Hsiao, Daniel Goldbach, Jiahao Li et al.
- A Robust Battery Pack State-of-Health Estimation Method with Cloud Data Based on Voltage-Controlled Charging Segment and Virtual Battery
Limei Wang, Xu Ran, Mengjie Jin et al.

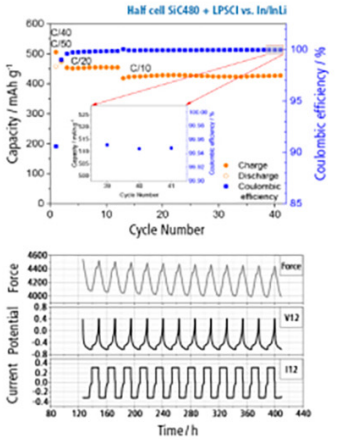
The New PAT-Cell-Solid!

EL-CELL®
electrochemical test equipment

Cycle Solid-State Batteries Under Controlled Pressure of up to 300 MPa (6 mm Diameter)!



- Adjust and measure a force of up to 9000 N on the cell stack!
Force adjustment possible throughout the entire experiment
- Built-in force, and temperature sensors!
With optional gas pressure sensor and gas in- and outlet
- PAT-Solid-Core for easy assembly and reproducible results!
Press and cycle solid-state batteries with 6 or 10 mm electrode diameter
- Cableless and highly sealed battery test cell!
For precise long-term measurements of solid-state cell chemistries



Learn more on our product website:
Scan me!

Download the data sheet (PDF):
Scan me!

Or contact us directly:
+49 40 79012-734
sales@el-cell.com
www.el-cell.com

This content was downloaded from IP address 158.69.193.207 on 16/11/2026 at 19:27

Journal of The Electrochemical Society, 2026 **173** 010504

Deconvolution of an SoC- and SoH-Dependent Contact Resistance in a Multilayer Pouch Cell Using Impedance Spectroscopy

Simon Helmer,[1,*,z] Robert Morasch,[1] Philip Rapp,[2,*] Sven Friedrich,[2,*] Andreas Jossen,[2] and Hubert A. Gasteiger[1,]**

[1]*Technical University of Munich, TUM School of Natural Sciences, Department of Chemistry and Catalysis Research Center, Chair of Technical Electrochemistry, 85748 Garching, Germany*
[2]*Technical University of Munich, TUM School of Engineering and Design, Department of Energy and Process Engineering, Chair of Electrical Energy Storage Technology, 80333 Munich, Germany*

The electrical contact resistance between the electrode coating and the current collector of lithium-ion battery electrodes, a critical factor in battery performance, is influenced by the intrinsic properties of the active materials and the amount of conductive electrode additives. However, its role in impedance analysis of large-format cells is often overlooked due to the superposition of high-frequency inductive contributions and the lack of electrode-specific impedance data. In this study, the effect of electrode geometric area on the high-frequency impedance contributions, including contact resistance and stray inductance, is systematically investigated through impedance simulations and validated experimentally with lab-scale and large-format cells. The simulated impedance spectra demonstrate that increasing electrode area amplifies inductive contributions, complicating the detection and quantification of contact resistances. These findings are confirmed via full- and half-cell impedance analysis of cells having the identical microscale silicon-dominated anode and NCA cathode electrodes, comparing the impedance spectra of a 3.5 mAh Si||NCA T-cell, equipped with a micro-reference electrode, with those of a 5.5 Ah multilayer pouch cell. The results establish a direct correlation between the impedance spectra obtained for the lab-scale and the large-format cells, providing a framework for accurately interpreting high-frequency impedance features in large-format commercial lithium-ion battery cells.
© 2026 The Author(s). Published on behalf of The Electrochemical Society by IOP Publishing Limited. This is an open access article distributed under the terms of the Creative Commons Attribution 4.0 License (CC BY, https://creativecommons.org/licenses/by/4.0/), which permits unrestricted reuse of the work in any medium, provided the original work is properly cited. [DOI: 10.1149/1945-7111/ae2402]

Manuscript submitted September 12, 2025; revised manuscript received November 17, 2025. Published January 6, 2026.

With the growing demand for lithium-ion batteries (LIBs), particularly for battery-powered electric vehicles, in situ analysis tools to monitor the state of charge (SoC) and state of health (SoH) over the battery cycle life are becoming increasingly important.[1–4] Among these tools, interest in electrochemical impedance spectroscopy (EIS) as a non-invasive diagnostic method has steadily increased in recent years.[5,6] In particular, the investigation of large-format cells, including on-board systems in battery electric vehicles, and the deconvolution of the individual impedance contributions of anode and cathode are of great interest for original equipment manufacturers (OEMs).[7] For this purpose, equivalent circuit models (ECMs) are commonly employed to analyze impedance data. However, the evaluation of measurements obtained from conventional two-electrode setups poses challenges, as the resulting impedance spectra represent a convolution of the contributions from both electrodes. This convolution complicates the identification of the behavior of an individual electrode, particularly in SoC regions where anode and cathode contributions overlap,[5] as exemplified in the impedance spectrum of a 5.5 Ah multilayer pouch (MLP) cell shown in Fig. 1a (for frequencies from 3 kHz–0.1 Hz). At higher frequencies, inductive effects become dominant for large-format cells, impeding the identification of impedance features contributed by electrochemical processes.[8,9]

Equivalent circuit models are generally employed to analyze the impedance contributions of individual electrodes in large-format cells, typically employing *R*/*C* circuit elements – a resistor and a capacitor in parallel – that are connected in series.[5] The most significant electrochemical features, such as those occurring at the interfaces of the active materials and the electrolyte for both the anode and the cathode, are typically represented by these *R*/*C*-elements. In this case, *R* describes the charge transfer resistance of a faradaic reaction (R_{ct}), while *C* describes the electrochemical double-layer capacitance (C_{dl}). In the case of lithium-ion battery anodes, contributions from the solid electrolyte interphase (SEI) may either be modeled separately from the charge transfer reaction (i.e., the lithium (de)intercalation) as a high-frequency contribution,[3,10] or may be contained in the R_{ct}/C_{dl} element of the anode.[11] In most cases, a constant phase element (CPE) *Q* replaces the ideal capacitor to account for non-idealities in the system. Additionally, an ohmic high-frequency resistance (R_{hf}) is connected in series to capture contributions from the ionic resistance in the electrolyte phase of the separator and the electrical resistance in the system (e.g., the resistance in the external wiring of the cell). A Warburg diffusion element (Z_{wb}) describes low-frequency diffusion effects, while inductive contributions from measurement cables and current collectors are modeled using an inductor (*L*) in series. These components, exemplified in Fig. 1b, form the basis of ECMs that are widely used for the impedance analysis of large-format cells, with numerous variants developed to model the impedance spectra of such cells (for an extensive review see Ref. 7).

Among the various ECM elements, the high-frequency resistance R_{hf} plays a central role in capturing ohmic losses in a battery cell. In various publications, the high-frequency *x*-axis intercept (i.e., where $-\mathrm{Im}(Z) = 0$) is found to shift with SoC and to gradually increase over cycle life.[2–4,12,13] These changes are typically linked to changes in the actual R_{hf} value, which is conventionally associated with the ionic resistance in the separator and the other purely electrical resistances (e.g., of the current collectors, the welding seams, and the connections). While an increase of the R_{hf} value over cycle life can be reasoned to be due to an actual aging-induced increase of the ionic resistance in the separator, the possible underlying cause of an SoC-dependent variation of the R_{hf} value remains unclear. A study by Xie et al. on commercial NCA cylindrical cells suggests that this behavior can be explained by an SoC-dependent contact resistance, which was incorporated into their impedance model.[14] However, further investigation is required to validate this hypothesis and determine its implications for the impedance analysis of large-format cells.

At the lab-scale cell level, reference electrodes (e.g., a gold wire micro-reference electrode (GWRE) in a T-cell setup) can be used to effectively distinguish between the individual impedance contributions of the anode and cathode electrodes to the full-cell impedance spectra.[15–17] Figure 1 highlights the disparity in the information that can be gained from EIS measurements of a large-format cell (Fig. 1a)

*Electrochemical Society Student Member.
**Electrochemical Society Fellow.
zE-mail: simon.helmer@tum.de

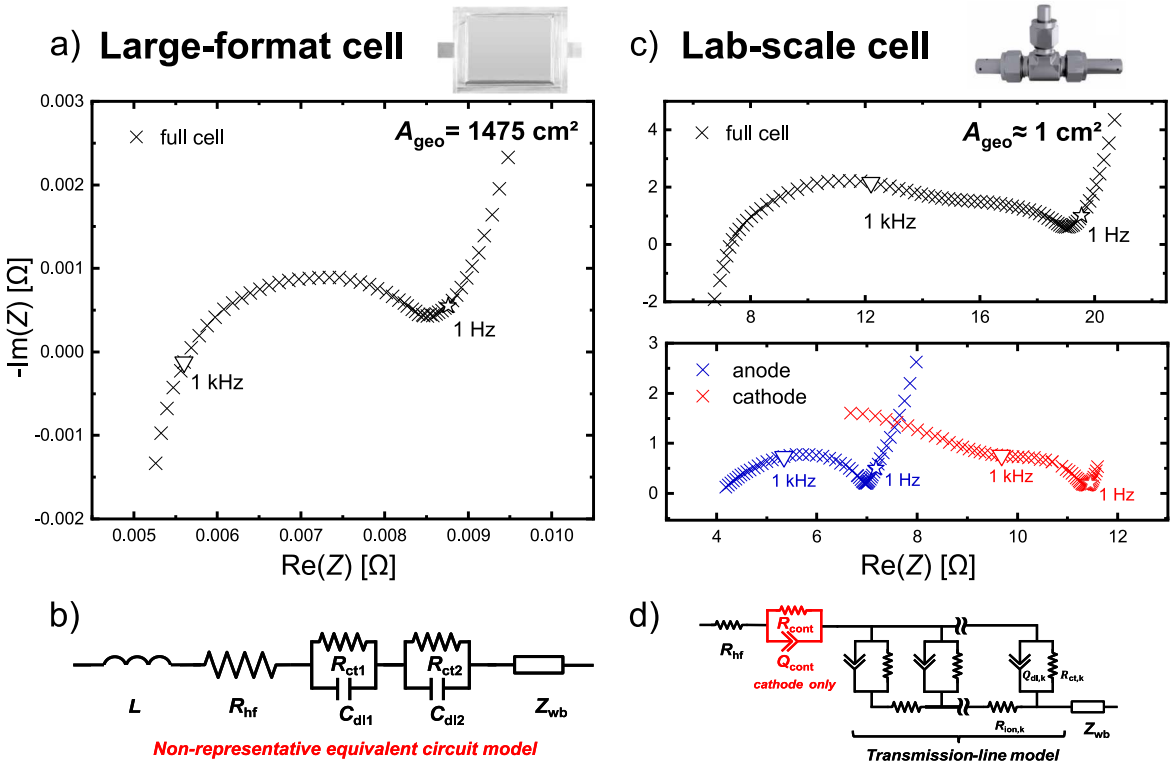


Figure 1. Impedance spectra obtained for a large-format cell and a lab-scale cell, assembled with the same microscale silicon-based anode and NCA cathode electrodes (see Experimental section) acquired at ∼50% SoC and 25 °C (the geometric electrode areas A_{geo} are given in the figure); also shown are the typical equivalent circuit models (ECMs). **(a)** Impedance response of a 5.5 Ah Si‖NCA multilayer pouch (MLP) cell in the frequency range from 3 kHz–0.1 Hz. **(b)** Frequently used ECM to model large-format cell impedances, with the *R*/*C* elements usually representing the electrochemical response of the cathode and the anode electrodes. **(c)** Impedance response of a 3.5 mAh Si‖NCA T-cell, measured either in full-cell configuration between 5 MHz–0.1 Hz (upper plot) or acquired via a gold wire micro-reference electrode (GWRE) that allows to record the individual impedance spectra of the anode (blue) and the cathode (red) between 30 kHz–0.1 Hz (lower plot). **(d)** Frequently used ECM to model individual electrode impedances, consisting of the simplified Levi transmission-line model (TLM) for a porous electrode and of an optional *R*/*C* element to account for a contact resistance between the electrode coating and the current collector (normally only used for cathode electrodes).

versus those of a lab-scale T-cell with a micro-reference electrode (Fig. 1c). The upper plot in Fig. 1c shows the full-cell impedance spectrum measured from 5 MHz to 0.1 Hz, while the lower plot presents the individual impedance spectra of the anode (blue) and the cathode (red) electrode (acquired only up to 30 kHz, due to experimental artefacts that arise at higher frequencies when using a GWRE, as described in Ref. 18). The latter allows for the electrode-resolved identification of key impedance contributions, such as the charge transfer resistance (R_{ct}) of the active material (AM) at mid-frequencies, as well as the high-frequency contributions like the ionic resistance across the electrolyte-filled pores of the electrode (R_{ion}) and the electrical contact resistance between the electrode coating and the current collector (R_{cont}). Detailed descriptions of the setup and guidance on how to analyze the electrode impedance responses can be found in the literature.[15,18–21]

The impedance of a conventional porous battery electrode is usually described by the simplified transmission-line model (TLM), which includes the ionic pathway through the porous electrode (R_{ion}) and the charge transfer either via the faradaic reaction (i.e., the lithium (de)intercalation, referred to as charge transfer resistance (R_{ct})) or via non-faradaic processes (i.e., the (dis) charging of the double layer capacitance (Q_{dl})), as shown in Fig. 1d. In addition to the ohmic resistance R_{hf}, an *R*/*C*-element representing the contact resistance between the electrode coating and the current collector (R_{cont}/Q_{cont}) can be incorporated in series to the TLM. The magnitude of such a contact resistance (R_{cont}) depends on the electrical conductivity of the AM, the amount of carbon additives, and the extent of external compression; it is generally more pronounced for cathode electrodes, owing to the poor electrical conductivity of most cathode active materials. For example, it is known that insufficient amounts of conductive additives such as carbon black (CB) in a cathode coating can lead to significant contact resistances, particularly upon extended charge/discharged cycling, which not only negatively affects the cell performance, but also has a significant effect on the high-frequency impedance response of the electrode.[22,23] So far, however, contact resistances have hardly been taken into account in the analysis of large-format cells. It seems plausible that this omission is due to the dominance of inductive contributions at high frequencies (above 1 kHz–10 kHz) in large-format cells, which makes it difficult to directly detect or even quantify the presence of contact resistances, which is the subject of this study.

This article is structured as follows. First, in the Theory section, we investigate the influence of the electrode's geometric surface area on its impedance response through a model-based approach, with a particular focus on the high-frequency resistance components, including contact resistance (R_{cont}) and stray inductance. Next, we describe the experimental setup, detailing the electrode compositions and the assembly of the MLP- and the T-cells, as well as the employed electrochemical measurement techniques. In the Results and Discussion section, we begin by comparing the impedance responses of the MLP-cell and of the T-cell under blocking conditions (i.e., in the absence of a charge transfer reaction), elucidating the dominant contributions to the high-frequency impedance spectra. Subsequently, the SoC dependence of the contact resistance and the charge transfer resistance in the T-cell with a micro-reference electrode is analyzed to deconvolute the individual contributions of anode and cathode. A comparative evaluation of ECMs is then carried out to assess the influence of a cathodic contact resistance on the impedance analysis of the MLP-cell. Finally, the

evolution of contact resistance over extended cycling is discussed, emphasizing the impact on long-term cell performance and aging diagnostics in large-format cells. We note that a silicon-based anode was employed due to the broader project targets next-generation lithium-ion battery materials, while the phenomena and the conclusions drawn here are anode-independent and therefore equally applicable to graphite-based cells.

Theory

In this section, the influence of the geometric surface area of an electrode on the high-frequency impedance will be examined via simulation of the impedance response of an idealized electrode with a small geometric area (1 cm^2), representing a lab-scale cell, versus one with a large electrode area (1000 cm^2), representing a large-format cell.

Typically, when examining impedance spectra of large-format cells, the dominance of inductive effects is observed above frequencies of ~1 kHz−10 kHz,[5] as illustrated in the impedance spectra of Fig. 1a. Several factors contribute to these inductances, including internal and external sources. Internally, inductances arise from the arrester tabs and from the current collectors within the cell, which are influenced by the cell design and the electrode geometry (e.g., wound jelly-roll versus stacked electrodes). For cylindrical cells, these complex inductive effects have been investigated in-depth, which are affected by the jelly-roll winding and by the tab alignment.[9,24] Consequently, inductive elements are being integrated into the corresponding equivalent circuit models that are used to analyze the impedance response, whereby internally caused inductances are typically addressed by placing inductive element within the TLM.[8,24] Externally caused inductances like stray inductances from the wiring between the potentiostat and the cell (e.g., self-inductance and mutual inductance) can also affect the impedance response, especially in low-impedance cells;[5,25] these are commonly represented by an inductor connected in series with the equivalent circuit of the electrochemical and electrical domains (see Fig. 1b).

These inductive elements are frequently modeled by a non-ideal inductor $Z_L(f)$, whose magnitude increases with frequency and is described by:[26]

$$Z_L(f) = (j\cdot\omega)^{\alpha_L}\cdot L_\alpha \quad [1]$$

Here, j is the imaginary unit, f is the frequency, $\omega = 2\pi f$ is the angular frequency, α_L is the constant phase exponent, and L_α is the non-ideal inductance (with $\alpha_L = 0-1$). For $\alpha_L = 1$, Eq. 1 reduces to the impedance of an ideal inductor ($Z_L(f)$ is thus defined analogously to the constant phase element Q). The term non-ideal inductor is used throughout this manuscript to refer to an inductor described by Eq. 1; the non-ideal inductor elements in the various presented ECMs are labelled by L.

Inductances have a more pronounced impact on large-format cells compared to lab-scale cells, due to differences in the overall cell impedance. In large cells, the impedance contributions from the electrochemical processes are in the low mΩ range, primarily due to the high geometric electrode area, which often exceeds 1000 cm^2 (exemplified in Fig. 1a). In contrast, a typical lab-scale cell has an electrode area of ~1−20 cm^2,[18,27] resulting in electrochemical impedance contributions in the Ω range, as evidenced in Fig. 1c (note the different scales of the axes in Figs. 1a and 1c). This distinction arises because a 1000-fold increase of the electrode area reduces the absolute resistances (i.e., R_{hf}, R_{ct}, and R_{ion}) by a factor of 1000 and increases the absolute double layer capacitance (Q_{dl}) by a factor of 1000. However, inductive effects linked to larger current collectors and multiple electrode layers tend to increase with size, while external stray inductance contributions remain constant. The latter can be estimated theoretically by the self-inductance of a straight cylindrical wire according to Eq. 2,

$$L = 0.2\cdot l\cdot\left[\ln\left(4\frac{l}{d} - 0.75\right)\right]\mu H \quad [2]$$

Here l is the wire length and d its diameter.[28] For typical potentiostat wire dimensions ($l \approx 15$ cm, $d \approx 0.5$ mm), this equation yields an inductance of approximately 0.1 μH. In summary, as the electrode area increases, the absolute inductive contributions remain constant or become more pronounced, while the relative impact of electrochemical impedance features diminishes (i.e., the impedance of the resistive and the capacitive elements scale with $Z_R \propto 1/A_{geo}$ and $Z_Q \propto 1/A_{geo}$, respectively). This trend is demonstrated in the following impedance simulations of an idealized porous electrode, which explores the variation of the relationship between inductive and electrochemical impedance contributions upon an increase of the geometric electrode area.

Figure 2 illustrates the simulated impedance spectra of porous model electrodes with a contact resistance at the current collector/electrode coating interface under blocking conditions (i.e., in the absence of faradaic reactions).[29] Figure 2a shows the simulated spectra, using the typical parameter values for a lab-scale electrode with a geometric electrode area of $A_{geo} = 1$ cm^2, with the values of the various equivalent circuit elements listed in the middle column of Table I. The gray line shows the spectrum simulated between 1 MHz to 10 Hz, using the ECM depicted in Fig. 1d (including the R_{cont}/Q_{cont} element; adopted from Landesfeind et al.[15]); the impedance of this circuit is given by Eq. 3 (in this case, the value of L_α is set to zero; with $R_{ion} = \sum r_{ion}$, and $Q_{dl} = \sum q_{dl}$).

$$Z(f) = (j\omega)^{\alpha_L}\cdot L_\alpha + R_{hf} + \frac{R_{cont}}{R_{cont}\cdot Q_{cont}\cdot(j\omega)^{\alpha_{cont}} + 1} + \sqrt{\frac{R_{ion}}{(j\omega)^{\alpha_{dl}}\cdot Q_{dl}}}\coth\left(\sqrt{R_{ion}\cdot(j\omega)^{\alpha_{dl}}\cdot Q_{dl}}\right) \quad [3]$$

To explore the impact of an increased electrode area, simulating a large-format model electrode with $A_{geo} = 1000$ cm^2, the resistances and the capacitances were scaled by the A_{geo}-ratio, i.e., the absolute resistances were divided by a factor 1000 and the absolute capacitances multiplied by 1000; the α values were kept constant (see right-hand column in Table I). The resulting impedance spectrum for the 1000 cm^2 model electrode is depicted by the gray line in Fig. 2b (again, using Eq. 3 with $L_\alpha = 0$). As expected, the shape of the spectra of the 1 cm^2 and the 1000 cm^2 model electrodes are identical, the only difference being the 1000-fold lower impedance values of the latter.

In order to examine the effect of cell inductance on the simulated impedance spectra (gray lines in Fig. 2), we added a non-ideal inductor L to the ECM in Fig. 1d (added in series, i.e., to the R_{hf} element), representing an external stray inductance with the above estimated value of $L_\alpha = 0.1$ μH $s^{(\alpha_L-1)}$ and an α_L value of 0.98. These values reflect those of a typical lab-scale cell, and similar values are also observed in our experimental MLP-cell data and align with the literature.[8]

The thus simulated spectrum for the 1 cm^2 lab-scale cell, depicted by the light blue line in Fig. 2a, features a high-frequency inductive contribution (resulting in negative −Im(Z) values), followed by the contact resistance semi-circle and a subsequent 45°-line region, representing 1/3 of the ionic resistance of the electrolyte phase within the electrode pores; at even lower frequency, the capacitive blocking branch is observed. Comparing the lab-scale electrode spectra with and without inductive contribution (light blue versus gray lines in Fig. 2a), it can be seen that the spectra are identical below 10 kHz. However, above 10 kHz, the influence of the inductance becomes evident, reflected in a slight shift of the high-frequency semi-circle towards lower imaginary values. This results

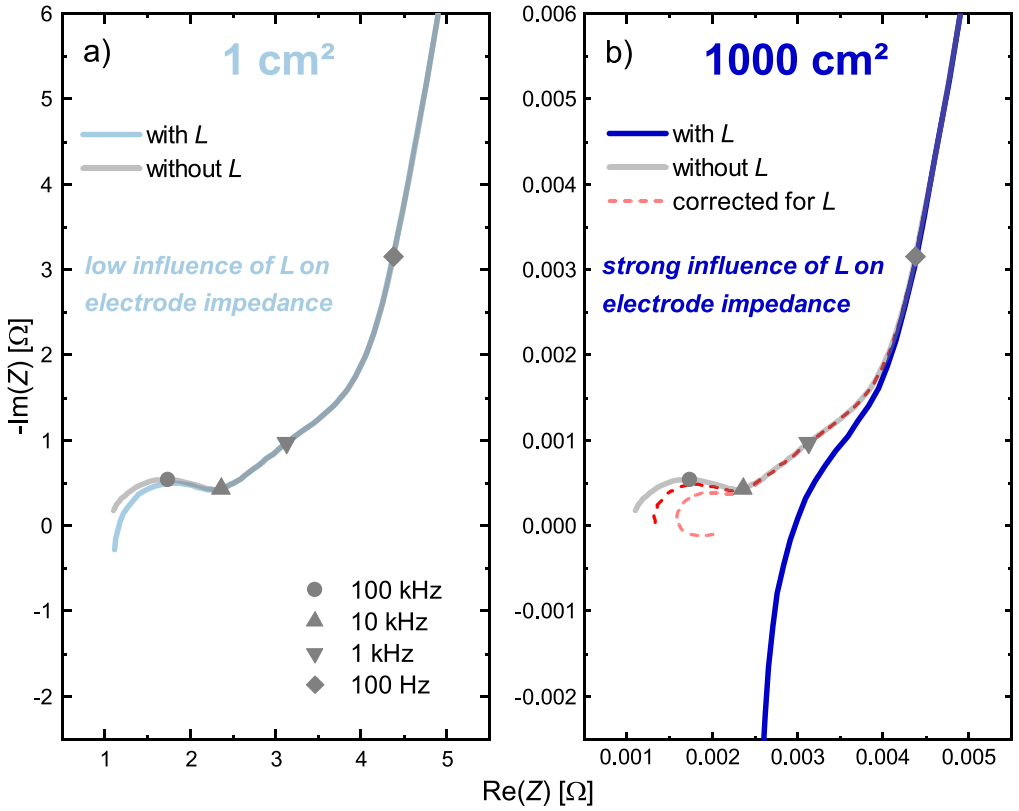


Figure 2. Simulated impedance spectra (1 MHz–10 Hz) of porous model electrodes with contact resistance under blocking conditions, using the parameters listed in Table I and the ECM in Fig. 1d (including the R_{cont}/Q_{cont} element and an additional non-ideal inductor L placed in series with the R_{hf} element). The electrochemical parameters of the 1 cm^2 lab-scale model electrode are scaled by a factor of 1000 for the 1000 cm^2 large-format electrode, i.e., the resistances are divided by 1000 and the capacitances multiplied by 1000, while the α values and L_α are kept constant. **(a)** Lab-scale electrode impedance (A_{geo} = 1 cm^2): the light blue line shows the spectrum with inductance, the gray line without. **(b)** Large-format electrode impedance (A_{geo} = 1000 cm^2): the dark blue line includes the inductance, the gray line excludes it; this highlights the increasing influence of L on the spectrum as the electrode area increases. The red dashed lines show L-corrected spectra, using the L_α and α_L values obtained first from a high-frequency fit of the dark blue spectrum to an ECM with in series connected L and R_{hf}^* elements (L+R_{hf}^* ECM), done either between 1−0.5 MHz (dark red) or between 0.5−0.35 MHz (light red). This reveals the increasing impact of the R_{cont}/Q_{cont} element as the fitting range to estimate L_α and α_L shifts to lower frequencies.

Table I. Parameters used in Eq. 3 to calculate the impedance responses shown in Fig. 2, simulating spectra for model electrodes with a contact resistance under blocking conditions, representing either a lab-scale electrode with A_{geo} = 1 cm^2 or a large-format electrode with A_{geo} = 1000 cm^2. For this, the resistance and capacitance values that are typical for a lab-scale electrode were scaled by the electrode area ratio in order to project the values for the large-scale model electrode, i.e., the resistances were divided by 1000 and the capacitances were multiplied by 1000; the α value and the value of L_α were kept constant.

Parameter	Lab-scale electrode (A_{geo} = 1 cm^2)	Large-format electrode (A_{geo} = 1000 cm^2)
L_α	0.1 μH $s^{(\alpha_L-1)}$	0.1 μH $s^{(\alpha_L-1)}$
α_L	0.98	0.98
R_{hf}	1 Ω	1 mΩ
R_{cont}	1 Ω	1 mΩ
Q_{cont}	5 μF $s^{(\alpha_{cont}-1)}$	5 mF $s^{(\alpha_{cont}-1)}$
α_{cont}	0.90	0.90
R_{ion}	6 Ω	6 mΩ
Q_{dl}	1 mF $s^{(\alpha_{dl}-1)}$	1 F $s^{(\alpha_{dl}-1)}$
α_{dl}	0.90	0.90

in an *apparent* high-frequency resistance, defined as the high-frequency x-axis intercept, of $R_{hf,app}$ = 1.2 Ω, which is 0.2 Ω higher than the actual R_{hf} value of 1.0 Ω that was used in the simulation (see Fig. 2a). Thus, if the simulated impedance spectrum were to be analyzed with an ECM that does not consider the inductive contribution, the extracted "R_{hf}" value would be overestimated by 20% in this example.

The effect of the very same non-ideal inductance on the simulated impedance spectrum of the 1000 cm^2 large-format model electrode, depicted by the dark blue line in Fig. 2a, is much more dramatic. At high frequencies, the pronounced effect of the inductance in case of the 1000 cm^2 model electrode blurs out the contact resistance semi-circle and the pore resistance feature, which were clearly distinguishable in the simulated spectrum without the L element (gray line in Fig. 2b). This leads to a ∼3-fold higher *apparent* high-frequency resistance of $R_{hf,app}$ = 3 mΩ compared to the actual R_{hf} value of 1 mΩ that was used in the simulation. Thus, the $R_{hf,app}$ value includes the entire contact resistance (R_{cont} = 1 mΩ) and a minor part of the ionic resistance value (R_{ion} = 6 mΩ) that were used in the simulation. As a consequence, when trying to determine the R_{hf} value from the measured impedance data of a large-format electrode (or cell), the cell inductance must be taken into account.

In practice, one way to estimate the inductance of a large-format cell is to first independently fit the impedance data at very high frequencies, where the inductive contribution to the impedance is very large compared to the contributions by the contact and the ionic resistance. In order to illustrate this approach, the high-frequency data of the simulated impedance of the large-format model electrode (blue line in Fig. 2b) were fitted to a simple ECM, consisting of an L and an R_{hf}^* element in series (referred to as L+R_{hf}^* ECM), exemplarily performing the model fit either in the frequency range

between 1−0.5 MHz or between 0.5–0.35 MHz. For the former range, this fit yields $L_\alpha \approx 0.099\,\mu H\ s^{(\alpha-1)}$. $\alpha_L \approx 0.98$, and $R_{hf}^* \approx 1.35\,m\Omega$, while for the latter range $L_\alpha \approx 0.098\,\mu H\ s^{(\alpha-1)}$, $\alpha_L \approx 0.98$, and $R_{hf}^* \approx 1.62\,m\Omega$ are obtained. Thus, the higher the selected frequency, the more accurately can the non-ideal inductor parameters be determined.

Subtracting the thus estimated L_α and α_L values from the originally simulated spectrum (dark blue line) results in the L-corrected spectra shown as dashed red lines in Fig. 2b (dashed dark red line for the 1–0.5 MHz range; dashed light red line for the 0.5–0.35 MHz range). Comparing these with the simulated spectrum obtained without the L element (gray line) reveals that the deviation decreases as the fitting range for the $L+R_{hf}^*$ ECM is extended to higher frequencies (dashed dark red line). This improvement arises because the impedance contribution of the R_{cont}/Q_{cont} element becomes increasingly dominant at lower frequencies, biasing the inductance estimation and leading to lower L_α values in the $L+R_{hf}^*$ ECM fit (see above). Thus, performing the $L+R_{hf}^*$ ECM fit at higher frequencies is beneficial to reduce the influence of contact impedance elements. However, in practical measurements, expanding the fitting range to higher frequencies is typically limited by the decreasing accuracy of conventional potentiostats/impedance analyzers with increasing frequency, particularly for low-impedance systems such as batteries. Therefore, for the later on conducted analysis of the experimental impedance data of large-format MLP-cells, a fitting window of 0.5–0.3 MHz was selected as a compromise between the accuracy with which the L_α and α_L values can be determined via the $L+R_{hf}^*$ ECM fit and the instrumental measurement constraints.

Using the $L+R_{hf}^*$ ECM fit in the 0.5–0.35 MHz range for the simulated spectrum in Fig. 2b (blue line), an L-corrected high-frequency resistance of $R_{hf} = 1.62\,m\Omega$ is obtained (reflecting the above determined high-frequency resistance of the $L+R_{hf}^*$ ECM fit). While this value is still ∼1.6-fold larger than the actually used R_{hf} value of 1.0 mΩ for the 1000 cm^2 model electrode (see Fig. 2b), it still is a significant improvement over the ∼3-fold larger $R_{hf,app}$ value of 3.0 mΩ that is obtained without the L-correction. Therefore, the R_{hf}^* value obtained from the L-corrected spectrum still provides a more accurate approximation of the actual R_{hf} value.

In summary, the here conducted impedance simulations of 1 cm^2 and 1000 cm^2 model electrodes demonstrate that the impedance spectra progressively lose high-frequency information related to R_{hf}, R_{cont}, and R_{ion} with increasing geometric electrode (and cell) area, caused by the increasing dominance of inductive contributions over the lower overall electrode (and cell) impedance.

Experimental

Electrode preparation and multilayer pouch cell assembly.— The electrode production and multilayer pouch cell assembly took place on the pilot-scale production line at the Institute for Machine Tools and Industrial Management (*iwb*) of the Technical University of Munich (TUM). Details on the production process are described by Schreiner et al.[30] for a comparable pilot-line campaign using graphite electrodes.

The here used anode electrode consists of 69.7 wt% microscale silicon active material (with $d_{50} = 4.5\,\mu m$ and $A_{BET} = 2.9\,m^2\,g^{-1}$; CLM 00001, Wacker Chemie AG, Germany), 19.9 wt% graphite (with $d_{50} = 2.5\,\mu m$ and $A_{BET} = 23.2\,m^2\,g^{-1}$; KS6L, Imerys, Switzerland), 8.2 wt% lithium-polyacrylic-acid (LiPAA) binder, 2 wt% conductive carbon black (CB) (Super-C65, Imerys, Switzerland), and 0.2 wt% carboxymethyl-cellulose (CMC) (Nippon Paper Industries, Japan). The cathode electrode consists of 96 wt% NCA cathode active material ($LiNi_{0.8}Co_{0.15}Al_{0.05}O_{1.985}(BO_3)_{0.01}$, BASF, Germany), 2 wt% CB (Super-C65, Imerys, Switzerland), and 2 wt% polyvinylidene-fluoride binder (PVdF, Solef 5130, Solvay, Belgium).

Two electrode configurations were prepared on the pilot-scale production line, all of them with cathode areal capacities of 3.75 mAh cm^{-2}_{NCA} (based on the reversible specific capacity of 185 mAh/g_{NCA}): (1) For the lab-scale T-cell measurements, single-side coated electrodes were used, with a cathode coating thickness of 76 ± 1 μm and porosity of 39.9 ± 1.1%; the corresponding anode coating had thickness of 45.0 ± 1.0 μm and a porosity of 52.0 ± 0.8 %.[31] (2) For the MLP-cells, double-sided electrodes were used, with a per-side coating thickness of 74.2 ± 0.8 μm and porosity of 36.5 ± 1%; the corresponding anode coating had a thicknesses of 45.9 ± 1.0 μm and a porosity of 49.0 ± 0.9%.[32] Here, it should be noted that the cathode coating porosity of the cathodes is relatively high compared to the typical ∼30% of commercial cathodes, and that the porosity of the single-side coated cathodes (39.9 ± 1.1%) is significantly higher than that of the double-side coated cathodes (36.5 ± 1%).

For MLP-cell assembly, electrodes were stacked by z-folding using a Celgard 2500 separator (Celgard LLC, USA), consisting of 11 double-sided anode electrode sheets (10.4 cm × 7.6 cm = 79.04 cm^2) and of 10 double-sided cathode electrode sheets (10.1 cm × 7.3 cm = 73.73 cm^2). The latter determine the effective total geometric electrode area of $A_{geo} = 1475\,cm^2$, which is used to normalize the MLP-cell impedances. The MLP-cells are filled with 1 M $LiPF_6$ in FEC:DEC 1:4 (v:v) (battery grade, Gotion, China). The total amount of electrolyte ($V_{electrolyte}$) added to the Si‖NCA MLP-cells was set to a pore volume filling factor of 1.5, i.e., to a value corresponding to 1.5 times the total pore volume of the electrodes and the separator in the cell (V_{pores}), resulting in 14.5 ml electrolyte for the 5.54 ± 0.09 MLP-cells (2.6 ml Ah^{-1}).

T-Cell assembly.—For the T-cells, single-layer coated anode and cathode electrodes (see above) were punched out to a diameter of 10.95 mm (equating to $A_{geo} = 0.94\,cm^2$), using an electrode punch (Hohsen Corp. OSAKA, Japan). A three-electrode cell setup (Swagelok® T-cell) with a gold wire micro-reference electrode (GWRE; for details see Ref. 18) was used for electrochemical impedance analysis. The GWRE was positioned centrally and approximately equidistant between working and counter electrodes to ensure a symmetric field; correct placement is critical to minimize artefacts.[18,33] Beyond the gold-wire design, established micro-reference formats include LTO- and Li/LiAl electrodes.[34,35] All cell components, including T-cell parts were dried in an oven at 70 °C for at least 12 h. The glass fiber (GF) separators (250 μm thick; VWR, Germany) were dried under dynamic vacuum in a vacuum oven (Büchi, Switzerland) at 300 °C overnight, before being transferred into an Ar-filled glovebox (25 ± 1 °C, oxygen and water content <0.1 ppm, Ar 5.0, Westfalen; MBraun, Germany). The cells were built inside the glove box, using two 11 mm diameter glass fiber separators and 70 μl of electrolyte (1 M $LiPF_6$ in FEC:DEC 1:4 (v:v); battery grade, Gotion, China). Using a potentiostat (SP-300, Biologic Science Instruments, France), the gold wire reference electrode was lithiated at 150 nA for 1 h via the counter electrode in a temperature-controlled chamber (25 ± 0.1 °C, Binder).

Cell formation, stabilization, and impedance measurements.— After the electrolyte filling, cell sealing, and a two-hour wetting period, the MLP-cells were clamped in a customized cell holder with a pressure of 0.2 MPa.[32] Prior to formation, potentiostatic electrochemical impedance spectroscopy (PEIS) measurements were performed under blocking conditions with a potentiostat (standard cable length; SP-300, Biologic, France). The PEIS measurements were performed in a four-point measurement configuration with 5 mV excitation from 500 kHz to 0.1 Hz. Analogously, for the T-cells with GWRE, PEIS measurements with 10 mV excitation were performed in full-cell configuration from 5 MHz to 0.1 Hz as well as in a three-electrode configuration (i.e., using the GWRE) from 30 kHz to 0.1 Hz in order to determine the individual electrode impedance contributions.

After the initial PEIS, the cells underwent one formation cycle and nine stabilization cycles; PEIS measurements were then recorded

in 10% SoC increments between 2.8–4.2 V. The full protocol and voltage profiles are shown in Appendix Fig. A·1 and described in the corresponding appendix subsection on formation and stabilization.

Data simulation and fitting.—Impedance fitting and simulations were performed with the impedance analysis software RelaxIS and Circuit Simulator (rhd instruments, Germany).

Electrolyte extraction for NMR analysis.—Electrolyte was extracted from cycled MLP-cells using the method reported by Hartmann et al.[36] (slightly modified from the earlier procedure developed by Thompson et al.[37]). For this, charge/discharge cycled MLP-cells were opened in an Ar-filled glovebox, and then ∼15 g of acetonitrile containing 5 wt% of an internal standard (1,4-Bis (trifluoromethyl)benzene, 98%, Sigma-Aldrich, Germany) were added via a 20 ml syringe. Subsequently, the cells were re-sealed and placed on an automatic shaker for 7 days in order to ensure complete mixing of the electrolyte and the added solvent. After 7 days, the cells were re-opened in an Ar-filled glovebox and the electrolyte/solvent/internal standard mixture was extracted from the cells. For NMR measurements, 0.9 ml of the mixture and 0.1 ml of acetonitrile-d3 (>99.8%, Sigma-Aldrich, Germany) were mixed and transferred to an airtight, FEP-lined NMR tube.

NMR analysis.—Quantitative ^{19}F and ^{1}H-NMR measurements were performed using a Bruker Avance 500 MHz spectrometer. The internal standard and the known quantity of acetonitrile solvent were used for the quantification of FEC and DEC. Both spectra were recorded with 64 scans with a 5 s relaxation delay.

Results and Discussion

Comparison of the MLP- and T-cell impedance spectra before formation.—Prior to cell formation, impedance measurements were performed under blocking conditions (achieved the very large charge transfer resistances at OCV prior to formation).[29,38] Figure 3a shows the cell impedance blocking spectra of a 5.5 Ah Si||NCA MLP-cell (black pluses) and of a 3.5 mAh Si||NCA T-cell (gray crosses), which reflect the combined impedance response of both electrodes (note that the components and areal capacities of the MLP- and the T-cells are identical). To enable a direct comparison, the spectra are normalized to their respective geometric areas (MLP-cell: 1475 cm^2, T-cell: 0.94 cm^2). Here, the upper frequency limits for the MLP- and the T-cell cell impedance measurements are set to 500 kHz and 5 MHz, respectively. The higher accessible frequencies in the T-cell measurements arise from its larger overall impedance, so that it remains within the potentiostat's high-frequency accuracy range (<3% error) even at 1 MHz. In contrast, the much lower impedance of the large-format MLP-cells restricts the upper frequency limit for measurement errors of ⩽3% to ∼500 kHz. In both cases, the measured inductance is likely dominated by stray inductances in the measurement setup (see Theory section).

The MLP-cell impedance (black pluses in Fig. 3a) exhibits two dominant features, similar to the trends observed in the simulated large-format cell (Fig. 2b): an inductive branch above 1 kHz (marked by the red open triangle), a capacitive branch at ∼100 Hz (marked by the gray open diamond), and a steep transition region in between. In contrast, the cell impedance spectrum of the T-cell (gray crosses), with the highest frequency point at 5 MHz, shows a semi-circle at high frequencies ($f_{apex} \approx 100$ kHz; marked by the gray open circle), followed by the convoluted ionic pore resistance ($f \approx$ 1–10 kHz) and a capacitive blocking branch at lower frequencies (∼100 Hz). It should be noted that the low-frequency blocking branches of the T-cell and MLP-cell spectra are shifted relative to each other, with the MLP-cell showing a ∼4 Ω cm^2 lower real impedance. This is ascribed to the lower ionic resistance of the Celgard 2500 separator in the MLP-cells ($t_{sep} = 25$ μm, with a porosity $\varepsilon_{sep} \approx 55\%$, and a tortuosity of $\tau_{sep} \approx 2.5$)[29] compared to that of the two glass fiber separators in the T-cells (at the ∼0.2 MPa compression, $t_{sep} \approx 2 \times 170$ μm thickness, $\varepsilon_{sep} \approx 90\%$, and $\tau_{sep} \approx 1$),[31] mostly due to the large difference in separator thickness. Further differences may also be influenced by the different cell design.

Figure 3b depicts the individual electrode impedance spectra acquired in the 3.5 mAh Si||NCA T-cell via the micro-reference electrode (GWRE) under blocking conditions. While the silicon anode spectrum (blue crosses) exhibits transmission-line model behavior for blocking conditions across the entire frequency range, the NCA cathode spectrum (red crosses) displays a striking difference at high frequencies. There, a pronounced semi-circle dominates the spectrum above ∼1 kHz, which can be attributed to the contact resistance (R_{cont}) between the NCA electrode coating and the aluminum current collector. In the present case, R_{cont} is rather large, which we ascribe to the relatively high NCA coating porosity of the single-side coated cathodes ($\varepsilon \approx 40\%$) and to the low amount of conductive additive (2 wt% C65) in the coating, possibly further aggravated by incipient interfacial delamination. A more detailed analysis of the origin and the consequences of contact resistances at the cathode can be found in earlier studies.[22,23,39] Beyond optimizing CB loading and fabrication parameters (e.g., calendering, drying, binder distribution) the use of carbon-coated/primed current collectors can substantially reduce cathode-side R_{cont} by improving electronic percolation.[39,40]

The ionic pore resistances of the electrodes were extracted from the blocking spectra of the individual electrodes, using the ECM depicted in Fig. 3c, which incorporates a simplified TLM and a high-frequency resistance (note that no inductor is included, as its contribution is insignificant up to 30 kHz for the only 0.94 cm^2 electrode area)[29,41]; for the fitting of the cathode spectrum, an additional R_{cont}/Q_{cont} element was taken into account, yielding $R_{cont} = 3.3 \pm 0.6\ \Omega\ cm^2$. All reported T-cell values represent the average of two independently measured cells, with the error margins reflecting the variability between them. The fitted values of R_{hf} and R_{ion} for both electrodes as well as the values of Q_{cont} and α_{cont} for the cathode are listed in Table II; the higher R_{ion} value for the cathode is ascribed mostly to its ∼2-fold larger thickness. The cathode contact resistance feature at high frequencies that is clearly assignable in the cathode impedance spectrum in Fig. 3b is reflected by the high-frequency semi-circle observed at an apex frequency of ∼100 kHz in the cell impedance spectrum of the T-cell (see Fig. 3a).

As pointed out in the introduction, the significant deviation of the MLP- from the T-cell blocking spectrum at frequencies above 1 kHz can be attributed to the large difference in the geometric electrode areas ($A_{geo,MLP\text{-}cell} = 1475$ cm^2 versus $A_{geo,T\text{-}cell} = 0.94$ cm^2). The much lower impedance of the MLP-cell (in the mΩ range) leads to overlaps of the cathode-side contact resistance and the convoluted ionic pore resistance with the inductive contributions. Consequently, the high-frequency x-axis intercept of the MLP-cell spectrum cannot be directly correlated to the high-frequency resistance R_{hf} but rather represents an *apparent* high frequency resistance $R_{hf,app}$. It is important to note that the cathode-side contact resistance strongly depends on cell compression,[31,32] so that minor differences in cell compression between MLP- and T-cells might lead to significant differences in their cathode-side R_{cont} values (even in view of the nominally identical cell compression of ∼0.2 MPa). Nevertheless, it is reasonable to assume that the MLP-cell also exhibits a significant cathode-side contact resistance.

To determine the inductive contribution to the MLP-cell impedance spectrum, with which one can construct an L-corrected blocking spectrum, the high-frequency data between 350–500 kHz of the MLP-cell spectrum in Fig. 3a were fitted to the L+R_{hf}^{*} ECM, as described in the Theory section. This yields $L_\alpha = 0.10 \pm 0.05\ \mu H\ s^{(\alpha_L - 1)}$, $\alpha_L = 0.98$, and $R_{hf}^{*} = 5.0 \pm 0.3\ \Omega\ cm^2$. The reported values are based on two independently measured MLP-cells, with error margins

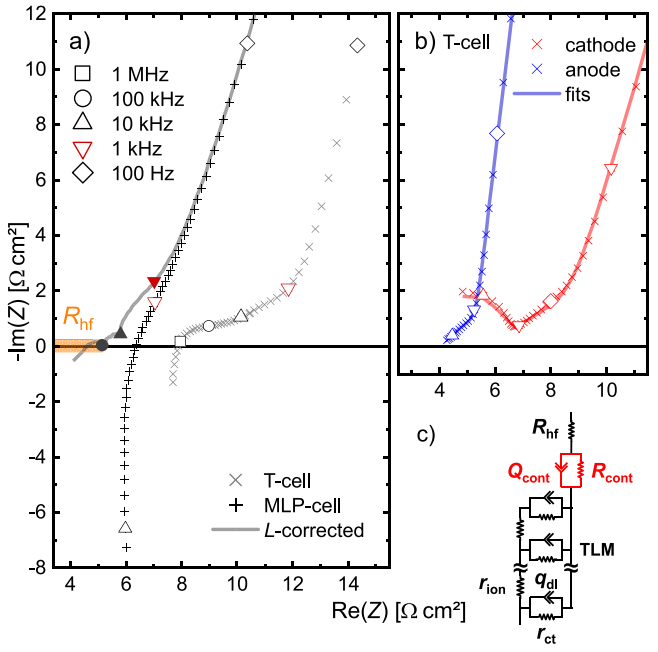


Figure 3. Comparison of the impedance spectra of a 5.5 Ah Si||NCA MLP-cell and a 3.5 mAh Si||NCA T-cell under blocking conditions before formation, with the cells being built with the same electrode materials and filled with 1 M $LiPF_6$ in FEC:DEC 1:4 (v:v) electrolyte. **(a)** Cell impedance spectra of the MLP-cell (black pluses) and of the T-cell (gray crosses), normalized to the respective geometric surface area of the cathode electrode ($A_{geo,MLP\text{-}cell} = 1475\ cm^2$, $A_{geo,T\text{-}cell} = 0.94\ cm^2$). The solid gray line shows the MLP-cell spectrum corrected by the stray inductance (L-corrected), with $L_\alpha = 0.1\ \mu H\ s^{(\alpha-1)}$ and $\alpha = 0.98$, extracted with an $L + R_{hf}^*$ fit of the high-frequency points between 350–500 kHz; the hatched orange area indicates the expected range of the "true" R_{hf} value of the MLP-cell. **(b)** Electrode-resolved impedance spectra acquired in the T-cell via the micro-reference electrode (GWRE) of the silicon anode (blue crosses) and the NCA cathode (red crosses); the solid lines are the impedance fits using the ECM depicted in panel c. **(c)** ECM used to fit the T-cell anode and cathode impedance spectra, with the high-frequency resistance R_{hf} and the contact resistance element R_{cont}/Q_{cont} (only used for the cathode) connected in series to a simplified TLM (with charge transfer resistances r_{ct}, constant phase elements q_{dl} that represent the double layer capacity, and ionic conduction resistances r_{ion} within the electrolyte-filled pores of the electrode).

reflecting the variability between them. The resulting L-corrected spectrum for the MLP-cell is shown by the solid gray line in Fig. 3a: it exhibits only a weak feature that is indicative of the pore resistance contribution (near ~1 kHz), while the cathode-side contact resistance that would be expected at higher frequences cannot be observed as a distinct feature. This suggests that the L_α value that was obtained by the $L+R_{hf}^*$ ECM fit between 350–500 kHz is either still biased by the R_{cont}/Q_{cont} contribution and/or that inductive contributions that originate from the stacked current collectors[8] may play a role. This, unfortunately, illustrates the limitations of the $L+R_{hf}^*$ ECM fit-based approach.

Nevertheless, as the high-frequency resistance value obtained from the $L+R_{hf}^*$ fit ($R_{hf}^* = 5.0 \pm 0.3\ \Omega\ cm^2$) must contain smaller contributions from the R_{cont} and R_{ion} features than the apparent high-frequency resistance (i.e., the high-frequency x-axis intercept) of the as-measured impedance spectrum ($R_{hf,app} = 6.2 \pm 0.1\ \Omega\ cm^2$; see black plusses in Fig. 3a), R_{hf}^* provides a reasonable upper limit for the actual high-frequency resistance R_{hf} of the MLP-cell. However, the R_{hf}^* value can vary depending on the frequency range for which it was obtained: the higher the frequency range, the smaller will be the contributions from R_{cont} and R_{ion}, but the larger will be the measurement error of the potentiostat. Furthermore, even for the simulated blocking spectrum of the 1000 cm^2 model electrode that was based on a well-defined inductor (see blue line in Fig. 2b), the L-corrected spectra (dashed red lines in Fig. 2b) based on the high-frequency $L+R_{hf}^*$ fit resulted in a 62% higher R_{hf}^* compared the actual R_{hf}. Therefore, also the here obtained R_{hf}^* that is also not entirely free of the contributions from R_{cont} and R_{ion} is likely an overestimate of the actual R_{hf} and should be considered an upper limit for R_{hf}.

A lower R_{hf} limit can be determined from the pure separator resistance, determined in an additional pouch-cell experiment with the CG 2500 separator placed between two current collector foils and wetted with the same electrolyte (following the procedure given Ref. 29), yielding $R_{sep} = 3.5 \pm 0.2\ \Omega\ cm^2$. This constrains the actual R_{hf} (corresponding to $R_{sep} + R_{el}$) of the MLP-cell to a range of 3.5–5.0 $\Omega\ cm^2$, which is marked by the hatched orange area in Fig. 3a. The remaining uncertainty are the electrical resistance contributions R_{el}, which are due to the electrical resistances of the current collectors, the welding seams, and the arrester tabs in a multilayer pouch cell,[42,43] but which are likely small compared to R_{sep}. Consequently, the orange dashed area in Fig. 3a represents the likely range of R_{hf}, derived from the above estimated upper and lower limits. However, the fact that the *apparent* high-frequency resistance of the uncorrected MLP-cell spectra ($R_{hf,app} = 6.2 \pm 0.1\ \Omega\ cm^2$) is not so much higher than the estimated R_{hf} range (~3.5–5.0 $\Omega\ cm^2$) suggests that the cathode-side contact resistance in the MLP-cell before formation must be relatively small.

In the following section, we will examine the evolution of the impedance spectra after formation as a function of SoC, aiming to estimate the contributions of the cathode-side contact resistance (R_{cont}) and of the anode and cathode charge transfer resistances ($R_{ct,an}$ and $R_{ct,ca}$). Given the lack of reliable reference values for the electrical resistance contributions R_{el} to R_{hf}, the upper estimated limit for the value of R_{hf} of 5.0 $\Omega\ cm^2$ (i.e., the value of R_{hf}^* determined from $L+R_{hf}^*$ ECM fit between 350–500 kHz) was set as a fixed value for the fitting of the MLP-cell impedance spectra after formation.

Comparison of the cell impedances of the MLP- and T-cells after formation.—SoC-dependent PEIS measurements were conducted after the initial formation and stabilization cycles as well as after the capacity-determination cycle (following the same procedure as that described for a T-cell in Fig. A·1). Figure 4a depicts the Nyquist plots of the cell impedance spectra of the Si||NCA MLP-cell, normalized to the geometric electrode area ($A_{geo} = 1475\ cm^2$), both in blocking conditions before formation (black crosses; corresponding to the black pluses in Fig. 3a) and after formation/stabilization, acquired at 0%, 50%, and 100% SoC (i.e., during the

Table II. Parameters determined from the fitting of the anode and cathode impedance spectra acquired for the 3.5 mAh Si||NCA T-cells with GWRE under blocking conditions (exemplary data shown in Fig. 3b), using the ECM shown in Fig. 3c (excluding the R_{cont}/Q_{cont} element for the anode). Values represent the mean of two independently measured cells, with errors indicating cell-to-cell variability.

	R_{hf} [Ω cm²]	R_{cont} [Ω cm²]	Q_{cont} [μF $s^{(\alpha_{cont}-1)}$ cm^{-2}]	α_{cont}	R_{ion} [Ω cm²]
anode	3.5 ± 0.4	—	—		4.3 ± 0.5
cathode	4.1 ± 0.3	3.3 ± 0.6	2.27 ± 1.01	0.82 ± 0.05	7.9 ± 0.9

green marked segment in Fig. A·1). The spectra after formation/stabilization at 0% and 100% SoC exhibit two distinct semi-circles in the mid-frequency range ($f \approx$ 1–0.1 kHz and $f \approx$ 100–1 Hz; for the 0% SoC spectrum, the latter can be seen in the zoomed-out view in Fig. A·2), while the spectrum at 50% SoC exhibits only one superimposed semi-circle ($f \approx$ 1 kHz–10 Hz). Additionally, all spectra drop below the x-axis intercept above $f \approx$ 1 kHz.

Compared to the blocking spectrum prior to formation, all post-formation spectra shift to substantially higher Re(Z) values, indicating an increased impedance. Furthermore, with increasing SoC, the high-frequency x-axis intercept, corresponding to $R_{hf,app}$, shifts to higher Re (Z) values: initially decreasing to a minimum at 70% SoC, before increasing again toward 100% SoC, as can be seen in Fig. A·2, where the spectra are shown for every 10% SoC increment. Similar SoC-dependent shifts of $R_{hf,app}$ have been reported for large-format commercial Li-ion battery cells.[3,12,13] For example, Kollmeyer et al. observed a comparable SoC-dependent shift of the high-frequency x-axis intercept in the impedance spectra of commercial graphite||NCA cells, which was interpreted as a change in R_{hf}.[13]

In comparison, Fig. 4b presents the Nyquist plots of the cell impedances of an Si||NCA T-cell. Contrary to what was observed for the MLP-cell (Fig. 4a), the high-frequency x-axis intercept before formation and after formation/stabilization, observed at $\approx$ 1.2 MHz, remains constant at $R_{hf,app} \approx 7.4\ \Omega\,cm^2$. Thus, for the T-cell cell impedance spectra, we assume that $R_{hf,app}$ must closely correspond to the actual R_{hf} (corresponding to $R_{sep} + R_{el}$), neglecting the minor influence of the cell inductance on the T-cell spectra, consistent with the above analysis of the simulated impedance spectra for a 1 cm^2 model electrode (see Fig. 2a). Consequently, another SoC-dependent parameter must be responsible for the SoC-dependent shift of the high-frequency x-axis intercept observed for the MLP-cell.

The cell impedance spectra of the T-cell (Fig. 4b) show three distinct semi-circles, most prominently observed at 0% and 100% SoC. A high frequency semi-circle with an apex frequency of $f_{apex} \approx$ 100 kHz (see inset) is followed by a semi-circle in the mid-frequency range ($f \approx$ 1 kHz–100 Hz) and another on at lower frequencies ($f \approx$ 100 Hz–1 Hz). Deconvoluting these processes at the lab-cell level, where a micro-reference electrode can be used to determine the individual anode and cathode impedance spectra, is essential for identifying the individual contributions to the cell impedance spectra of large-format cells, particularly for gaining a deeper understanding of how the x-axis intercept varies with SoC.

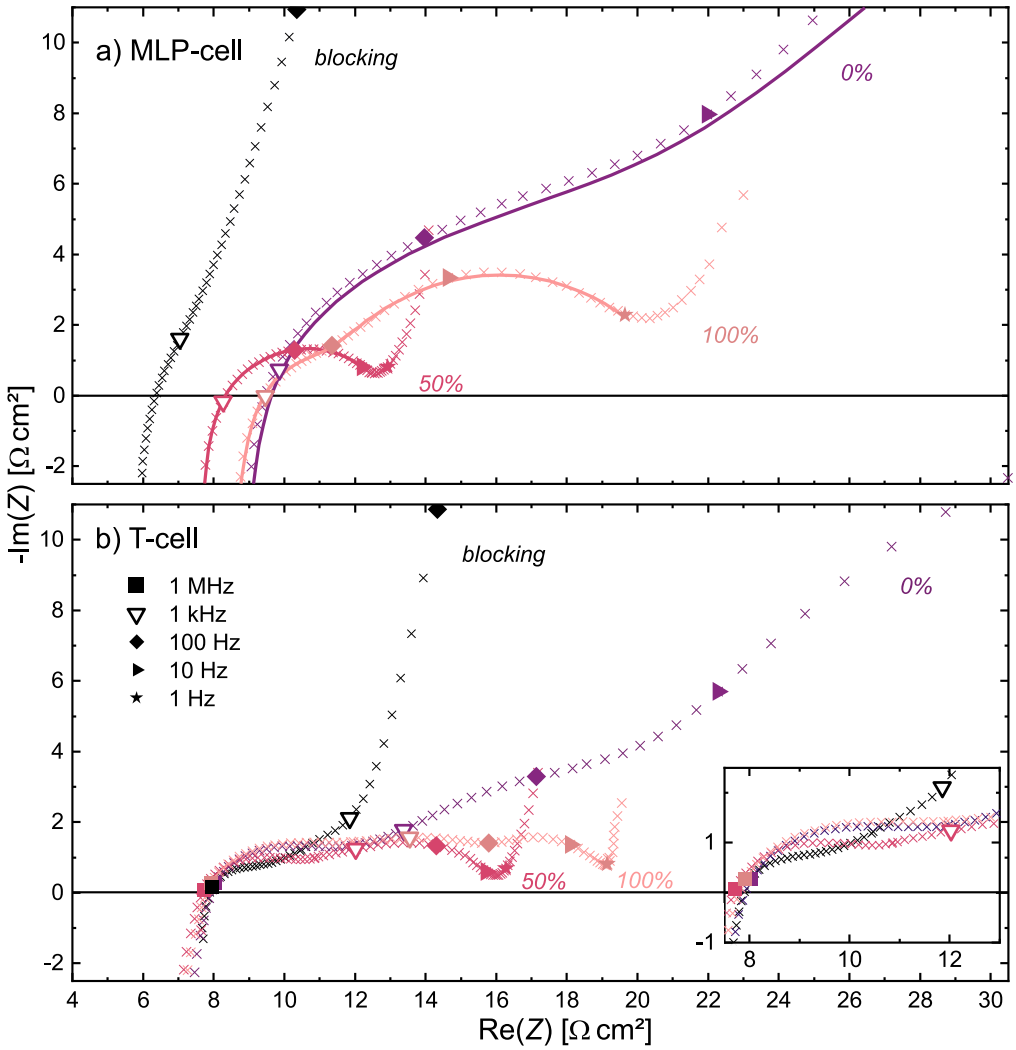


Figure 4. Nyquist plots of the cell impedances of a 5.5 Ah Si||NCA MLP-cell and a 3.5 mAh Si||NCA T-cell (built with the same electrode materials and 1 M $LiPF_6$ in FEC:DEC 1:4 (v:v) electrolyte) between 2.8–4.2 V_{cell} at 25 °C, acquired after formation/stabilization (see green marked segment in Fig. A·1) at 0, 50, and 100% SoC. **(a)** MLP-cell built with Celgard 2500 separator: PEIS data (symbols) acquired with an excitation amplitude of 5 mV between 500 kHz and 0.1 Hz; the solid lines are fits of the spectra using the ECM shown in Fig. 7b. **(b)** T-cell built with 2 GF separators: PEIS data (symbols) acquired with an excitation amplitude of 10 mV between 5 MHz and 0.1 Hz. The inset is a zoomed-in view of the data between 1 MHz and 1 kHz. Note that the blocking spectra for both cells correspond to those shown in Fig. 3a.

Deconvolution of anode and cathode impedances for T-cells via the GWRE.—Figure 5 presents Nyquist plots of the anode (blue crosses) and cathode (red crosses) impedances after formation/stabilization at 0%, 50%, and 100% SoC, measured for a T-cell via the gold wire μ-reference electrode (the associated cell impedances are shown in Fig. 4b).

At 0% SoC (Fig. 5a), the anode spectrum can be divided into three distinct regions: the ionic pore resistance slope at high frequencies (30–1 kHz), the anodic charge transfer resistance $R_{ct,an}$ at intermediate frequencies (1 kHz–10 Hz), and a capacitive increase attributed to diffusion contributions at lower-frequencies ($f < 1$ Hz). When increasing the SoC to 50% (blue crosses in Fig. 5b) and 100% (Fig. 5c, a decrease of $R_{ct,an}$ can be observed. It is important to note that $R_{ct,an}$ represents a combined contribution of the SEI resistances and of the charge transfer resistances of both the silicon and the graphite active materials in the anode electrodes. The latter is expected to play only a minor role, as the accessible graphite capacity within the applied voltage window (>170 mV versus Li^+/Li) is estimated to contribute less than 2% to the total anode capacity (≈53 mAh g_{Gra}^{-1} at >170 mV).[44] Furthermore, no significant shift of the projected high-frequency resistance can be observed in the anode impedance spectra, indicating that the conductive carbon additive network remains intact before and after formation/stabilization. This suggests that the electrode's electrical conductivity is sufficiently high, with the carbon additive network maintaining a proper conductive pathway.[45]

The cathode spectra exhibit two consecutive semi-circles across all SoCs. At 0% SoC (red crosses in Fig. 5a), corresponding to a cell voltage of 2.87 V_{cell} or a cathode potential of ~3.51 V versus Li^+/Li), the mid-frequency semi-circle ($f \approx 100$ Hz–1 Hz) dominates and represents the cathode charge transfer resistance ($R_{ct,ca}$). This semi-circle decreases rapidly with increasing SoC, but rises again towards 100% SoC where the cathode potential reaches ~4.33 V versus Li^+/Li (at 4.17 V_{cell}). The high-frequency semi-circle ($f > 1$ kHz), interpreted as the cathode-side contact resistance R_{cont}, is clearly more pronounced in the here shown spectra after formation/stabilization when compared to the cathode impedance spectrum prior to formation (see Fig. 3b). This behavior is consistent with observations made in our earlier studies with LNMO ($LiNi_{0.5}Mn_{1.5}O_4$) cathodes.[15,23] Furthermore, R_{cont} seems to be SoC-dependent, following a similar trend as $R_{ct,ca}$, which will be discussed in greater detail later.

Mapping the individual electrode contributions (Fig. 5) to the cell impedance response (Fig. 4b) of the T-cell will next be used to identify the electrode-specific features in the cell impedance spectra of the MLP-cell (Fig. 4a). As discussed above, the high-frequency semi-circle in the cell impedances can be ascribed to the cathode-side contact resistance, while the semi-circle at mid-to-low frequencies ($f \approx 100$–1 Hz) represents $R_{ct,ca}$; the semi-circle at intermediate frequencies ($f \approx 1$ kHz–100 Hz) can be attributed to the anode's $R_{ct,an}$.

The ECM used to fit the T-cell impedance data of the silicon anode and of the NCA cathode at different SoCs is shown in Fig. 3c. To improve the accuracy of fitted parameters, the number of free parameters was reduced through the following simplifications: (1) The R_{ion} values for the anode and cathode were fixed, based on the values listed in Table II, which were determined from the blocking spectra as described in Refs. 15 and 16. Although changes in the ionic resistance of the anode and cathode upon formation as well as SoC-dependent changes (e.g., due to the expansion of the silicon) are neglected, this approach ensures consistency.[17,20,21] (2) As only a fraction of the contact resistance semi-circle can be observed in the cathode impedance spectra with a frequency limit of 30 kHz (higher frequencies were shown to lead to artefacts in the spectra when obtained via the GWRE),[18] the R_{hf} value of the cathode ($R_{hf,ca}$) was determined by subtracting the more clearly defined R_{hf} value of the anode ($R_{hf,an}$) from that of the R_{hf} value obtained from the cell

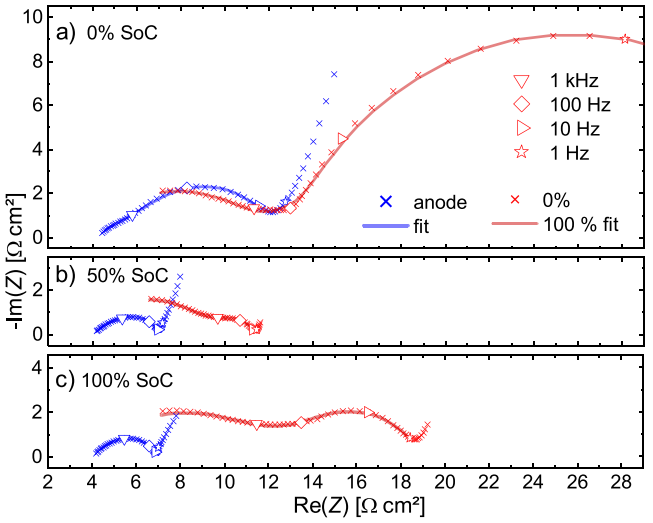


Figure 5. Nyquist plots of the SoC-dependent anode (blue crosses) and cathode (red crosses) impedances obtained at 25 °C for the 3.5 mAh Si||NCA T-cell via the GWRE after formation/stabilization (the associated cell impedances are shown in Fig. 4b). PEIS data were acquired at OCV between 30 kHz–0.1 Hz in 10% SoC steps from 2.8–4.2 V_{cell}. Exemplarily shown are: **(a)** 0% SoC; **(b)** 50% SoC; and, **(c)** 100% SoC. The anode charge transfer resistance $R_{ct,an}$ (blue crosses) decreases upon increasing the SoC from 0% to 100%; the cathode impedances exhibit a R_{cont} feature at high frequences and a cathode charge transport resistance $R_{ct,ca}$ at lower frequencies. The solid lines are fits of the spectra with the ECM in Fig. 3c, neglecting the low-frequency diffusional impedance contributions.

impedance ($R_{hf,cell}$; measurable up to 5 MHz, so that all cathode-side R_{cont}-based impedance contributions can be accounted for), i.e, $R_{hf,ca} = R_{hf,cell} - R_{hf,an}$. Here, the value of $R_{hf,cell}$ for the T-cells was $R_{hf,cell} = 7.4 \pm 0.2\ \Omega\ cm^2$ (taken as the high-frequency x-axis intercept of the cell impedance, see gray crosses in Fig. 3a). (3) Finally, the low-frequency diffusional contributions were excluded from the impedance fits; for this purpose, the low-frequency data points that were selected such that diffusive influences were negligible. Thus, the free fitting parameters are the R_{ct}, Q_{dl}, and α_{dl} values of anode and cathode, the R_{cont}, Q_{cont}, and α_{cont} values of the cathode, and the $R_{hf,an}$ value of the anode.

Figure 6a shows the SoC-dependent charge transfer resistance ($R_{ct,an}$) of the silicon anode in the T-cell, which decreases from ~10 Ω cm^2 at 0% SoC (corresponding to an anode potential of E_{an} = 0.65 V versus Li^+/Li) to 1.2 Ω cm^2 at 100% SoC. The cathode balancing limits the lithiation of the anode to ~1250 mAh g_{Si}^{-1} in the first cycle (corresponding to ~35% of the theoretical capacity of Si),[46] so that 100% SoC after formation/stabilization corresponds to $E_{an} \approx 0.16$ V versus Li^+/Li (at 4.17 V_{cell}).[47,48] A similar trend has been reported in other studies with microscale silicon anodes, i.e., a decreasing $R_{ct,an}$ as the anode potential is decreased towards 0.17 V versus Li^+/Li.[49,50] On the other hand, the SoC-dependent cathode charge transfer resistance ($R_{ct,ca}$) shown in Fig. 6c follows a characteristic U-shaped behavior, consistent with observations for other CAMs such as Ni-rich NCM811 ($LiNi_{0.8}Co_{0.1}Mn_{0.2}O_2$) and Li- and Mn-rich NCM.[51,52] At low SoC, minor variations in potential among individual cells can strongly affect the value of $R_{ct,ca}$, resulting in a higher cell-to-cell variation.

Figure 6b shows the cathode-side contact resistance after cell formation/stabilization, which ranges between ~8-13 Ω cm^2. This is higher by a factor of ~2.4–4 compared to the R_{cont} value prior to formation (see Table II), which can be attributed to the passivation of the electrode/current collector interface via the passivation of the Al current collector.[23,53] The here observed SoC-dependence appears to follow that of $R_{ct,ca}$: the highest R_{cont} value of ~13 Ω cm^2 is observed at 0% SoC (where E_{ca} = 3.51 V versus Li^+/Li), which then

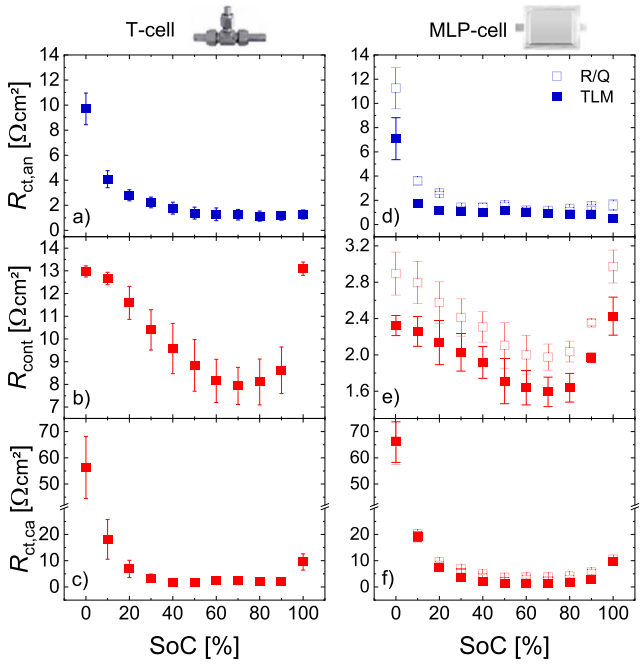


Figure 6. SoC-dependence of the anode and cathode charge transfer resistances ($R_{ct,an}$ and $R_{ct,ca}$) and of the cathode-side contact resistance (R_{cont}) of the Si‖NCA T-cell (3.5 mAh) and MLP-cell (5.5 Ah) after formation/stabilization at 25 °C (built with the same electrode materials and electrolyte). This is based on an analysis of the individual anode and cathode impedances obtained with the T-cell with GWRE (Fig. 5) as well as on the cell impedance of the MLP-cell (Fig. 4a). T-cell analysis: The anode and cathode spectra were evaluated with the ECM shown in Fig. 3c: **(a)** $R_{ct,an}$; **(b)** R_{cont}; and, **(c)** $R_{ct,ca}$. MLP-cell analysis: This was done using either the TLM-based ECM in Fig. 7a (filled squares) or the more simple ECM with R/Q-elements (Fig. 7b): **(d)** $R_{ct,an}$: **(e)** R_{cont}; and, **(f)** $R_{ct,ca}$. For better comparability, the resistances were normalized to the respective geometric electrode area (0.94 cm^2 for the T-cell and 1475 cm^2 for the MLP-cell). Two identical cells were tested, and the error bar represents the absolute deviation of their values from the mean.

decreases to a minimum value of ∼8 Ω cm^2 at 70% SoC (E_{ca} = 3.95 V versus Li^+/Li), followed by a sharp increase towards 100% SoC (where E_{ca} = 4.33 V versus Li^+/Li); this trend is observed for all investigated T-cells, even though the absolute R_{cont} values vary somewhat. Complementary experiments with graphite‖NCA T-cells using the same electrolyte (1 M $LiPF_6$ in FEC:DEC 1:4 (v:v)) showed a similar SoC-dependence of R_{cont} (data not shown), indicating that this behavior does not depend on the choice of anode electrode. A plausible cause for the U-shaped R_{cont} versus SoC relationship could be related to the dependence of the electrical conductivity of NCA on its lithium content (i.e., on its SoC), which increases monotonically with increasing SoC.[54] In this case, the rapid R_{cont} increase towards 100% SoC may be related to the SoC-dependent variation of the thickness of the NCA electrode, with a maximum thickness at ∼75% SoC (corresponding to $E_{ca} \approx$ 4.05 V versus Li^+/Li).[55] However, more investigations would be needed to validate this hypothesis.

Deconvolution of the MLP-cell impedance spectra.—For large-format cells such as the MLP-cell analyzed here, the cathode-side contact resistance semi-circle is not visible due to its overlap with inductive contributions (as illustrated in Fig. 3a), so that it is typically either neglected in the analysis of large-format cells or not considered to be an SoC-dependent parameter. However, based on the findings from the simulation of the model electrodes (see Fig. 2), on the comparison of the impedance spectra of the MLP- and the T-cell prior to formation (see Fig. 3a), and on the analysis of the electrode-resolved impedances of the T-cell via the GWRE after formation (see Fig. 5), the SoC-dependent shift of the high-frequency x-axis intercept observed for the cell impedance of the MLP-cell (see Fig. 4a) can be attributed to the SoC-dependence of R_{cont}.

While the R_{cont} semi-circle with an apex frequency of ∼100 kHz is clearly observed in the cell impedance of the 0.94 cm^2 electrode area T-cell (see Fig. 4b), it is overlapped in the 1475 cm^2 electrode area MLP-cell by the dominating stray inductance above ∼1 kHz. For this reason, subtracting the inductive contribution form the measured cell impedance of the MLP-cell to obtain the L-corrected spectrum (using the L_α and α_L values determined via the L+R_{hf}^* ECM fit between 0.5–0.35 MHz) does not result in a clear R_{cont}-related semi-circle prior to MLP-cell formation (gray solid line in Fig. 3a). Even after MLP-cell formation/stabilization, which in case of the T-cell leads to an increase of R_{cont} by a factor of ∼2.4–4 (see above), neither the as-measured spectrum (see black symbols in Fig. A·3) nor the L-corrected spectrum show a clear R_{cont}-related semi-circle (see black line in Fig. A·3). However, if R_{cont} is increased further, which can be achieved by lowering the cell compression,[22,32] the R_{cont}-related semi-circle appears in the L-corrected spectrum. This can be illustrated by lowering the MLP-cell compression to 0.05 MPa (4-fold lower than the here used standard compression of 0.2 MPa): while the R_{cont} feature is not visible in the as-measured cell impedance (see red symbols in Fig. A·3), a pronounced R_{cont}-related semi-circle can be seen in the L-corrected spectrum (see red line in Fig. A·3).

Even though the L-corrected spectra of the MLP-cell under the here used standard compression of 0.2 MPa do not show a clear R_{cont}-related semi-circle, it will be shown in the following that reasonable estimates for $R_{ct,an}$, $R_{ct,ca}$, and the cathode-side R_{cont} can be obtained via ECMs that contain an inductive element in series to R_{hf}. As noted in the introduction, the cell impedance analysis of large-format cells is typically performed using an ECM with multiple R/Q elements connected in series. Upon acquiring comprehensive electrochemical parameterization of individual electrodes of the Si‖NCA system through the above described analysis of T-cells with a micro-reference electrode, a more refined ECM can be established for the MLP-cells, thereby enhancing the fidelity of the interpretation of the impedance spectra.

Figure 7a presents the here proposed ECM, which captures the dominant processes from high to mid frequencies (∼1 Hz), comprising: 1. A non-ideal inductor L; 2. a high-frequency resistance R_{hf} element (representing the separator ionic resistance and electrical resistances); 3. a parallel R_{cont}/Q_{cont} element for the cathode, representing the cathode-side contact resistance; 4. a TLM for the anode electrode, including the ionic pore resistance $R_{ion,an}$ and the charge transfer resistance $R_{ct,an}$ as well as a constant phase element representing the double layer capacitance $Q_{dl,an}$; and, finally, 5. a TLM for the cathode, including $R_{ion,ca}$, $R_{ct,ca}$, and $Q_{dl,ca}$. This model will subsequently be compared to one of the commonly employed ECMs for large-format cells (neglecting the porous electrode structure), depicted in Fig. 7b: it includes an L and an R_{hf} element in series as well as three R/Q-circuits that represent the cathode-side contact resistance (1), the anode charge transfer resistance (2), and the cathode charge transfer resistance (3). In both models, the low-frequency impedance contributions are not accounted for. Given the large number of parameters, multiple fits that yield an apparently good fit of the experimental data are possible, so that the value of a given fitted parameter may not necessarily reflect its physical reality. In order to improve the fidelity of the model, several of the parameters were fixed prior to fitting the SoC-dependent cell impedance data of the MLP-cell after formation/stabilization, shown in Fig. 4a, to the ECMs given in Fig. 7: i) the R_{hf} value was set to the value of R_{hf}^* that was determined under blocking conditions using the L+R_{hf}^* ECM fit between 0.5–0.35 MHz (note that the L_α and α_L values were left as free fitting parameters); and, ii) the R_{ion} values, of the TLM-based model (Fig. 7a), for the anode and cathode electrode were fixed to those obtained from the T-cell measurements with the GWRE under blocking conditions (see Table II).

Before analyzing the SoC-dependent behavior of the fitted values of $R_{ct,an}$, $R_{ct,ca}$, and the cathode-side R_{cont}, the fitted values for the inductive element were compared between the two ECMs shown in

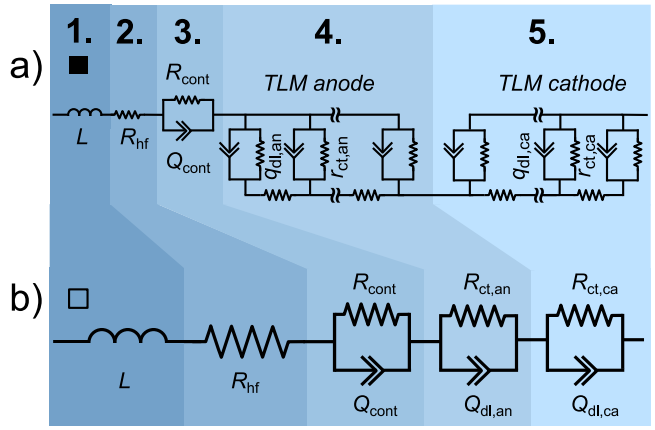


Figure 7. ECMs used to fit the SoC-dependent cell impedance spectra of the MLP-cell after formation/stabilization (shown in Fig. 4a), accounting for the the stray inductance (L), for the high-frequency resistance (R_{hf}) of the cell (i.e., the ionic resistance of the separator and electrical resistances), and the high-frequency contributions of the cathode-side contact resistance (R_{cont}/Q_{cont}). **(a)** ECM based on simplified TLMs for the anode and cathode electrode, including R_{ion}, R_{ct}, and Q_{dl} for each electrode. **(b)** ECM that neglects the electrode's porous structure and simplifies the anode and cathode contributions by an R/Q element for each. The results of the fits are shown in Fig. 6, with the filled squares using model a) and the open squares model b); for these fits, the R_{hf} value was set to the value of R_{hf}^{*} that was determined under blocking conditions using the $L+R_{hf}^{*}$ ECM fit between 0.5–0.35 MHz, and the R_{ion} values for anode and cathode were set to the values listed in Table II.

Fig. 7. Both yield nearly identical values after formation, with $L_\alpha = 0.14 \pm 0.02\ \mu H\ s^{(\alpha_L - 1)}$ and $\alpha = 0.98$, indicating that the inductive behavior is independent of the specific ECM. A slight increase in L_α compared to before formation values was observed, which can be attributed to the influence of the higher R_{cont} after formation. In the following, we will focus our analysis on the physically based model (Fig. 7a), which incorporates the behavior of porous electrodes via the use of TLMs. The SoC-dependent values of $R_{ct,an}$, $R_{ct,ca}$, and the cathode-side R_{cont} derived from the ECM depicted in Fig. 7a are shown in Figs. 6d, 6e (filled squares).

The anode charge transfer resistance $R_{ct,an}$ deduced from the cell impedance fit of the MLP-cells (see filled squares in Fig. 6d) starts with $\sim 8\ \Omega\ cm^2$ at 0% SoC and decreases to $\sim 1\ \Omega\ cm^2$ at 100% SoC. Within the experimental error, these values are consistent with those obtained from the anode impedance fit of the T-cell measurements using the GWRE (see Fig. 6d), except for a slightly steeper $R_{ct,an}$ decline between 20%-40% SoC in case of the MLP-based data. Similarly, the cathode charge transfer resistances $R_{ct,ca}$ deduced from the MLP-cell impedances (filled squares in Fig. 6f) are in rather good agreement with those obtained from the T-cell impedances (Fig. 6c), with only a minor discrepancy at 0% SoC. This is likely due to small variations in the OCV, which can significantly influence $R_{ct,ca}$, particularly at low and high SoC.

The cathode-side contact resistances R_{cont} deduced from the MLP-cell impedances (filled squares in Fig. 6e) are highest towards both SoC limits and exhibit a pronounced minimum at 70% SoC. This trend not only parallels the R_{cont} behavior deduced from the T-cell impedances (Fig. 6e), but also clearly reflects the SoC dependence of the high-frequency x-axis intercept (i.e., of $R_{hf,app}$) that can be observed for the MLP-cell impedance spectra (Fig. A·2). Overall, however, it has to be noted that the R_{cont} values deduced for the MLP-cells are ~4-fold lower than those for the T-cell. The most likely cause for this difference is the ~3.4% higher cathode coating porosity of the single-side coated cathode electrodes used for the T-cell measurement ($\varepsilon = 39.9 \pm 1.1\%$) compared to that of the double-side coated cathodes that were used for the MLP-cells ($\varepsilon = 36.5 \pm 1\%$) MLP-cell cathodes, which must have resulted from slight variations in the calendering process that initially had not been noted. Unfortunately, even such small changes in porosity can significantly affect the electronic contact resistance between the cathode coating and the aluminum current collector, particularly at the here used rather low carbon black content (2 wt%), leading to notable differences in R_{cont}.[22,23,29] As a result, it is not surprising that the R_{cont} values of the T-cell cathodes are higher than those of the MLP-cell cathode, so that a direct comparison of the absolute R_{cont} values between these two cell formats is not possible. However, the matching SoC-dependent R_{cont} trends suggest that both cell formats reflect the same underlying contact resistance behavior, enabling a meaningful relative comparison. This interpretation is further supported by the observation that porosity differences have little effect on the charge transfer kinetics R_{ct}, which show good agreement between both cell formats (see Fig. 6). Kinetics are not significantly influenced by porosity differences, as long as electronic connectivity between active material particles is maintained.[32] A minor contribution to the observed R_{cont} differences may stem from the fixed value of R_{hf} used in the fitting procedure of the MLP-cell impedances: here, the R_{hf}^{*} value obtained from the $L+R_{hf}^{*}$ ECM fit between 0.5–0.35 MHz was used as a fixed parameter (i.e., $R_{hf} \equiv R_{hf}^{*} = 5.0\ \Omega\ cm^2$); if the lower bound of R_{hf}, corresponding the measured separator resistance of $3.5\ \Omega\ cm^2$ (see orange hatched area in Fig. 3a) had been used, the impedance fit would result in $\sim 1.5\ \Omega\ cm^2$ higher R_{cont} values for the MLP-cells compared to those given in Fig. 6e.

The parameters derived from the ECM incorporating the anode and cathode TLMs (see Fig. 7a) exhibit consistent trends and comparable magnitudes to those obtained from the R/Q-circuit model (see Fig. 7b), as can be seen by comparing the filled and open symbols in Figs. 6d–6f. The R/Q-circuit based ECM leads to an even more closely aligned trend of the anode charge transfer resistances between the MLP- and the T-cells (open symbols of Fig. 6d and filled symbols of Fig. 6a), likely due to the reduced complexity of the R/Q-circuit model that does not include R_{ion}. Finally, to further check the plausibility of the fitted parameters, the capacitances derived from both models can be evaluated. Neglecting the α values of the CPEs, the capacitance values are estimated as $Q_{cont} \approx 5$ mF, $Q_{ct,an} \approx 1$ F, and $Q_{ct,ca} \approx 5$ F for both ECMs. Normalizing Q_{cont} to the current collector/electrode interface area of ($\sim 1475\ cm^2$), a surface area-normalized capacitance of $\sim 3\ \mu F\ cm^{-2}$ is obtained, consistent with the values reported for the double-layer capacitance.[15] Similarly, normalizing $Q_{ct,an}$ to the specific surface area of the Si composite anode ($\sim 45.8\ m^2$) and $Q_{ct,ca}$ to that of the NCA cathode ($\sim 44.7\ m^2$), surface area-normalized value of ~2 and ~11 $\mu F\ cm^{-2}$ are obtained, respectively, both of which are again reasonable values.

Evolution of the contact resistance in an MLP-cell upon cycling.—The presence of a cathode-side contact resistance R_{cont} in large-format cells becomes more apparent in the cell impedance spectra upon cell aging over the course of extended charge/discharge cycling. Figure 8 shows the evolution of the impedance spectra of a ~5.5 Ah Sill NCA MLP-cell acquired at 3.6 V_{cell} (≈50% SoC) over cycling. The MLP-cell (clamped at the standard compression of 0.2 MPa) was cycled at 25 °C between 2.8 V and 4.2 V. The cycling procedure, starting with initial formation/stabilization cycles and a rate-capability test, included sets of 20 cycles at 0.5 C, with periodic check-up cycles at 0.1 C and SoC-dependent rate capability tests at 2 C (for the detailed cycling procedure and the evolution of the capacity retention, represented by the state of health (SoH), see Ref. 32). Impedance measurements were performed between 200 kHz−0.1 Hz at each check-up at 50% SoC until an SoH of 70% (125 mAh g_{NCA}^{-1}) is reached.

At cycle 13, defined as 100% SoH, the Nyquist plot of the impedance spectrum at 50% SoC shown in Fig. 8 (left-most spectrum, orange crosses; same spectrum as that depicted in red in Fig. 4a) exhibits a single convoluted semi-circle, representing the combined anode and cathode contributions. The same spectral feature is also observed after the subsequent rate test (red crosses in Fig. 8), whereby a significant increase of the *apparent* high-frequency resistance ($R_{hf,app}$) is observed. Upon continued cycling to an SoH of 90% (purple crosses),

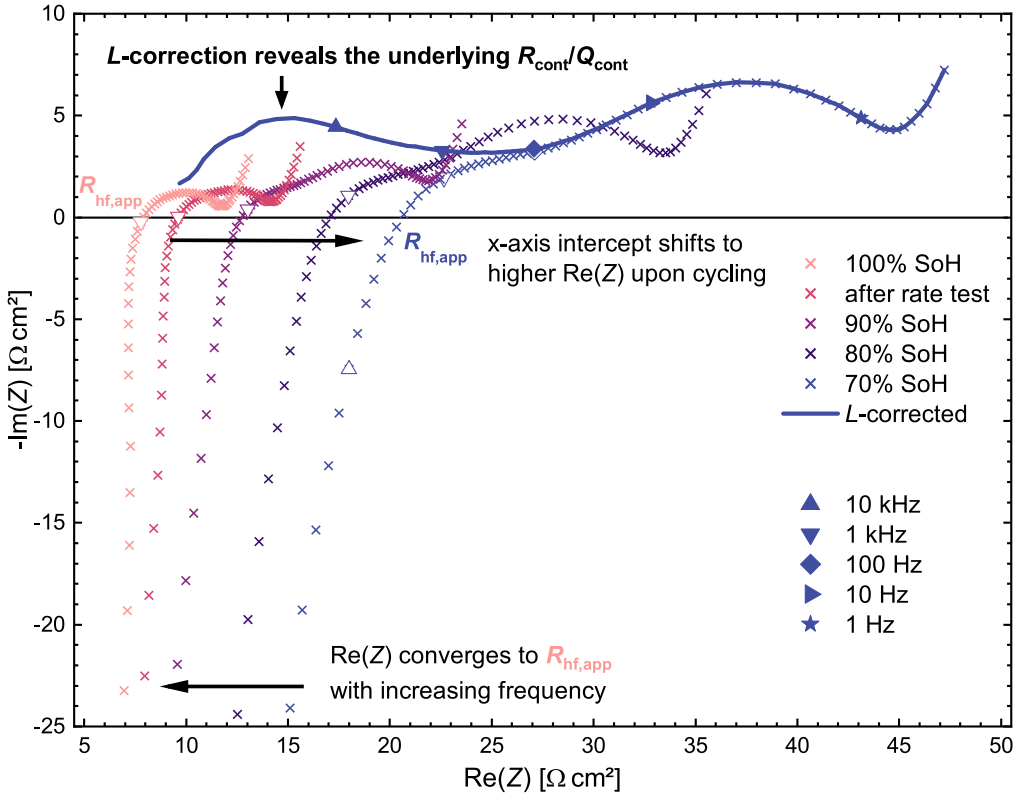


Figure 8. Cell impedance spectra (cross symbols; shown between ~30 kHz to 0.1 Hz) of a ~5.5 Ah Si||NCA MLP-cell at 25 °C, measured at 3.6 V (≈50% SoC) over the course of extended charge/discharge cycling (the cycling protocol and the associated capacity retention (≡ SoH) is given in Ref. 32). Depicted are the spectra obtained between 100% SoH (cycle 13, after initial formation/stabilization cycles) and 70% SoH (cycle 361). The $R_{hf,app}$ values marked in the figure indicate the high-frequency x-axis intercepts, which increase over cycling. The solid line depicts the *L*-corrected spectrum at 70% SoH from 100 kHz to 0.1 Hz, revealing the high-frequency cathode-side contact resistance-related semi-circle (R_{cont}/Q_{cont}). The spectra are normalized to the geometric surface of the cathode electrode of 1475 cm^2.

$R_{hf,app}$ shifts to higher Re(*Z*) values and the initially single convoluted semi-circle gradually separates into distinct kinetic contributions from both anode and cathode. The pronounced increase of $R_{hf,app}$ is observed until 70% SoH (blue crosses), which could be interpreted as a significant loss of $LiPF_6$ that has been observed for cell-storage at high SoC,[36] as electrolyte dry-out, and/or as an increased internal electric resistance.[2,3] For the 70% SoH spectrum, the stray inductance was estimated by fitting the $L + R_{hf}^{*}$ ECM in the 100–200 kHz range (for aged cells, the measurement protocol restricted the frequency window to 200 kHz), whereby the R_{hf}^{*} was fixed at $R_{hf}^{*} = 5.0\ \Omega\,cm^2$, which corresponds to the value determined from the pre-formation blocking spectrum (see black pluses in Fig. 3a); this yielded $L_\alpha = 0.17\ \mu H\,s^{(\alpha_L-1)}$ and $\alpha_L = 0.97$.Subtracting the thus determined inductance from the as-measured impedance spectrum results in the *L*-corrected spectrum at 70% SoH that is shown by the solid blue line in Fig. 8. This *L*-corrected spectrum at 70% SoH reveals an additional semi-circle at higher frequencies ($f \geqslant 10$ kHz), alongside spectral artifacts above 100 kHz that are omitted for clarity. Based on the findings and analysis so far, this emerging high-frequency semi-circle can clearly be attributed to an increase in the cathode-side contact resistance, aligning with earlier findings that showed an increase of the cathode-side contact resistance upon the cycling of LNMO-based cathodes, making use of T-cells with a GWRE.[23]

Post-mortem analysis of the MLP-cells ruled out electrolyte dry-out as a cause for the increase of $R_{hf,app}$ over cycling. The excess electrolyte used (with a pore volume filling factor of 1.5) provided a sufficient electrolyte reserve to prevent dry-out, as demonstrated by the essentially unchanged amount of DEC solvent in the MLP-cell that was determined via electrolyte extraction and NMR analysis (see gray bars in Fig. A·4); only the amount of FEC solvent decreased over cycling (see blue bars in n Fig. A·4), which is consistent with earlier studies that indicated the preferential consumption of FEC in LIB cells with silicon-dominant anodes.[56] This analysis furthermore showed that the $LiPF_6$ concentration remained essentially constant over cycling (see green bars in Fig. A·4).

These findings clearly indicate that the majority of the $R_{hf,app}$ shift observed in the impedance spectra of the MLP-cell over cycling (Fig. 8) must be primarily caused by the gradual increase of the cathode-side R_{cont} rather than by electrolyte dry-out or $LiPF_6$ depletion, suggesting that interfacial degradation or the mechanical contact changes at the interface of the cathode electrode coating with the current collector play a dominant role. A more detailed analysis of pressure-dependent R_{cont} evolution under different cell compression levels is reported in Ref. 32. Additional high-frequency impedance contributions caused by electrical degradation of the aged silicon composite electrode, such as the loss of conductive pathways within the silicon-dominant anode electrode, will be addressed in a forthcoming publication.[45] The *L*-corrected spectrum in Fig. 8 (70% SoH, blue solid line) underscores the critical importance of considering the impact of the cell inductance on the high-frequency impedance contributions in large-format cell upon cell aging.

Conclusions

This study demonstrates how the geometric electrode area governs the high-frequency impedance response of lithium-ion battery cells, with a particular focus on the interplay between the cathode-side contact resistance and the inductive contributions in large-format cells.

The simulated spectra for a 1000 cm^2 area model electrode under blocking conditions (based on the parameters listed in Table I) that are shown in Fig. 9 illustrate this interplay between inductive effects and the high-frequency (R_{hf}) and the contact resistance (R_{cont}). The black spectrum serves as a reference case (with $R_{hf} = 1\ m\Omega$ and

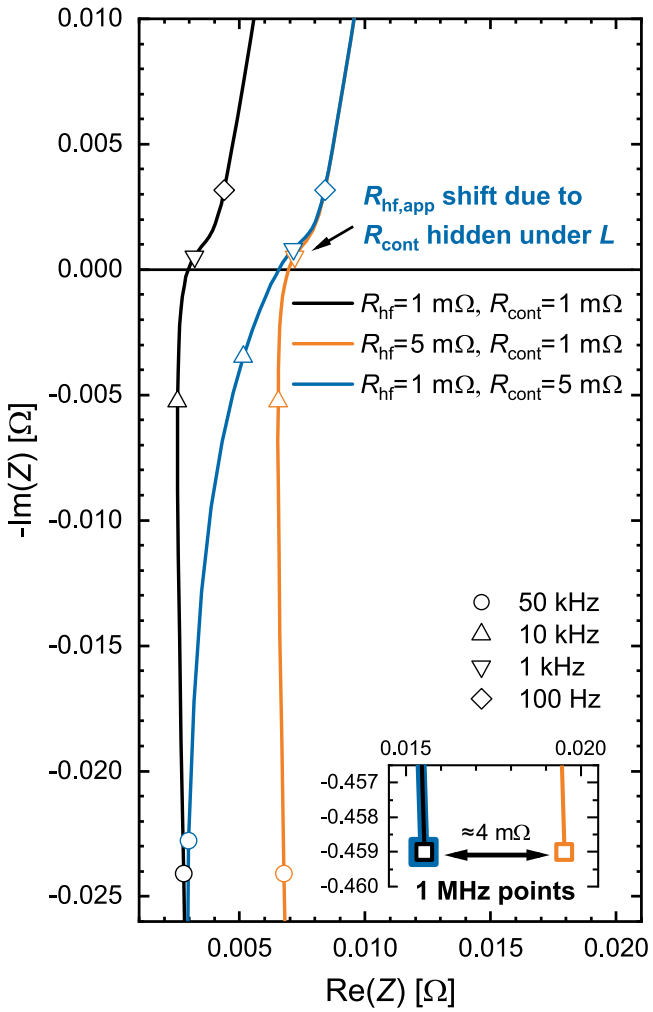


Figure 9. Simulation of the impedance spectra of a large-format model electrode under blocking conditions between 1 MHz−20 Hz using the ECM from Fig. 3c and the parameter values of Table I for a 1000 cm^2 model electrode area (right side), changing either the high-frequency resistance R_{hf} or the contact resistance R_{cont} while keeping the other parameters fixed. This demonstrates the influence of the inductivity on the impedance spectra of large electrode area electrodes, particularly in the high-frequency region: the black spectrum serves as a reference case (R_{hf} = 1 mΩ and R_{cont} = 1 mΩ; same as the blue spectrum depicted in Fig. 2b); the orange spectrum shows the effect of an increased high-frequency resistance (R_{hf} = 5 mΩ and R_{cont} = 1 mΩ); and, the blue spectrum shows the effect of an increased contact resistance (R_{hf} = 1 mΩ and R_{cont} = 5 mΩ). The impedances for these three spectra at 1 MHz are depicted by the inset.

R_{cont} = 1 mΩ) that was already shown and discussed in Fig. 2b (there depicted by the blue line). Increasing the ohmic resistance R_{hf} by a factor of 5 from 1 to 5 mΩ shifts the entire spectrum uniformly to higher Re(Z) values (orange spectrum in Fig. 9), whereas a 5-fold increase of the contact resistance R_{cont} from 1 to 5 mΩ instead results in a nearly 5-fold increase of the *apparent* high-frequency resistance $R_{hf,app}$ (similar to orange spectrum), far exceeding the actual R_{hf} value of 1 mΩ. This deviation originates from the inductance-overlapped R_{cont}/Q_{cont} contribution and manifests itself as a characteristic positive slope in the high-frequency branch between ∼10–50 kHz.

Impedance simulations in combination with experimental impedance investigations on Si||NCA cells, conducted with both lab-scale T-cells with ∼1 cm^2 area electrodes and with ∼1500 cm^2 area multilayer pouch (MLP) cells, revealed an *apparent* high-frequency resistance $R_{hf,app}$ for the MLP-cells that is substantially larger than their expected "true" high-frequency resistance (i.e., the sum of the ionic resistance of the separator and typical electrical resistances). A method was established to estimate the high-frequency resistance of MLP-cells under blocking conditions. In parallel, T-cell measurements after formation revealed an SoC-dependent cathode-side contact resistance, attributed to the low carbon black (C65) content and the relatively high electrode porosity. In contrast, for the MLP-cells, the inductive contribution to the impedance spectrum leads to an overlap with the cathode-side contact resistance, resulting in an SoC-dependent high-frequency x-axis intercept. Lowering the cell compression further amplified this effect, as the associated increase in R_{cont} causes the high-frequency intercept to shift to larger Re(Z) values. An increase of the cathode-side R_{cont} was also observed over the course of extended charge/discharge cycling, which resulted in an increase of the high-frequency x-axis intercept. This is often broadly attributed to electrolyte dry-out, conductive salt depletion, and/or a general rise of the internal cell resistance, but in fact is caused by the overlap of the inductive impedance contribution with the cathode-side contact resistance.

In summary, the combined experimental and simulation results underscore the necessity of electrode-level characterization to enable a reliable interpretation of large-format cell impedance spectra. A characteristic high-frequency slope in the Nyquist plot slope above ∼10−100 kHz in the positive imaginary part of a Nyquist plot is a key indicator of a superimposed high-frequency R_{cont}/Q_{cont} contribution in large-electrode area, low-impedance cells. Identifying this effect is essential for accurately interpreting high-frequency contributions in impedance spectra and distinguishing inductive artifacts from true electrode resistances in large-format cell aging studies.

Acknowledgments

S. H. gratefully acknowledges the financial support from the BMBF (Federal Ministry of Education and Research, Germany), under the auspices of the ExZellTUM III project (grant number 03XP0255). The authors want to thank the research battery production team of iwb at TUM, especially Alessandro Sommer, for manufacturing the electrodes and the multilayer pouch cells. We also thank Wacker Chemie AG for kindly providing the microscale silicon material (CLM 00001).

Appendix

Formation, Stabilization, and SoC-Dependent Impedance Measurement Protocol.—Figure A·1 illustrates the potential profile over the course of the initial formation and stabilization cycles of a 3.5 mAh Si||NCA T-cell with a GWRE between 2.8–4.2 V_{cell} at 25 °C. The formation process involves an initial constant current (CC) charge and discharge at a rate of 0.067 C, followed by five CC stabilization cycles at 0.1 C. Subsequently, four cycles were carried out at 0.2 C CC. These initial 10 cycles (shown in black in Fig. A·1) were conducted with a Maccor battery cycler (Series 4000, Maccor, USA). After this, a given cell was connected to a Biologic potentiostat (SP-300, Biologic, France), where a capacity-determination step was conducted at 0.1 C CC charge with a CV-hold at 4.2 V_{cell} (until the current decayed to below 0.02 C), followed by 0.1 C CC discharge to 2.8 V_{cell} (shown in red). This was followed by SoC-dependent full-cell PEIS measurements (5 MHz–0.1 Hz), starting at 2.8 V_{cell}, and then increasing the SoC in 10% increments using 0.1 C CC charge steps, each followed by 1 h OCV phases, after which the PEIS measurements were conducted (shown in green). Owing to the constraints imposed by the device and the gold wire reference electrode, the three electrode T-cell measurements are conducted in a subsequent charging cycle from 30 kHz–0.1 Hz. The same formation, stabilization, and SOC-dependent full-cell PEIS measurement procedure was also used for the MLP-cells.

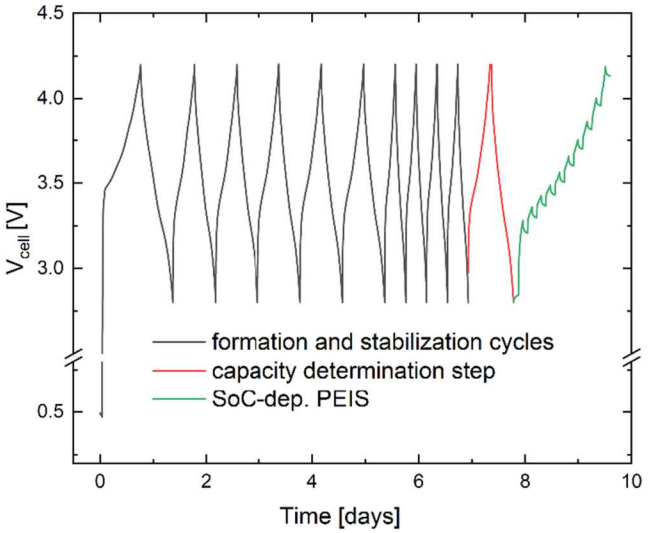


Figure A·1. Illustration of the potential profile over the course of the initial formation/stabilization cycles and the subsequent SoC-dependent PEIS measurements, exemplarily shown for a 3.5 mAh Si||NCA T-cell. Cycling was conducted between cell voltages of 2.8 and 4.2 V_{cell} at 25 °C. The initial formation cycle was a constant current (CC) charge/discharge at a rate of 0.067 *C*, followed by 9 CC stabilization cycles (5 at 0.1 *C* and 4 at 0.2 *C*). These were conducted with a battery cycler (Series 4000, Maccor). After these 10 initial cycles (marked in black), the cell was connected to a potentiostat (SP-300, Biologic), where the cell capacity was determined using a 0.1 *C* CC charge with a CV-hold at 4.2 V_{cell} (until the current decreased below 0.02 *C*) and a 0.1 *C* CC discharge to 2.8 V_{cell} (marked in red). This was followed by SoC-dependent PEIS measurements, starting at 2.8 V_{cell}, then increasing the SoC in 10% increments by 0.1 *C* CC charge steps, each followed by a 1 h OCV step and a subsequent PEIS measurement (marked in green).

Nyquist Plots of the SoC-Dependent Impedance of the MLP-Cell.—Figure A·2 is a zoomed-out view of the cell impedance spectra of the MLP-cell shown in Fig. 4a, depicting all the data in the frequency range from 100 kHz to 0.1 Hz (except the blocking spectra that are shown to only 20 Hz). The spectra were obtained at 10% SoC intervals after cell formation/stabilization (analogous to what is depicted for the T-cell in Fig. A·1); as reference, the blocking impedance spectrum prior to formation is also depicted in Fig. A·2. After cell formation/stabilization, all spectra exhibit a shift of the high-frequency x-axis intercept to higher Re(*Z*) values, i.e., an increased $R_{hf,app}$. However, when examining the spectra a different SoCs, a notable trend can be observed: starting from 0% SoC (blue crosses) and progressing towards higher SoCs, $R_{hf,app}$ decreases until 70% SoC (yellow crosses), after which increases again until 100% SoC (pink crosses). As elucidated in the main text, this SoC-dependent variation in $R_{hf,app}$ can be attributed to the influence of the cathode-side contact resistance, which is superimposed by the inductive contributions arising from the overall low cell impedance.

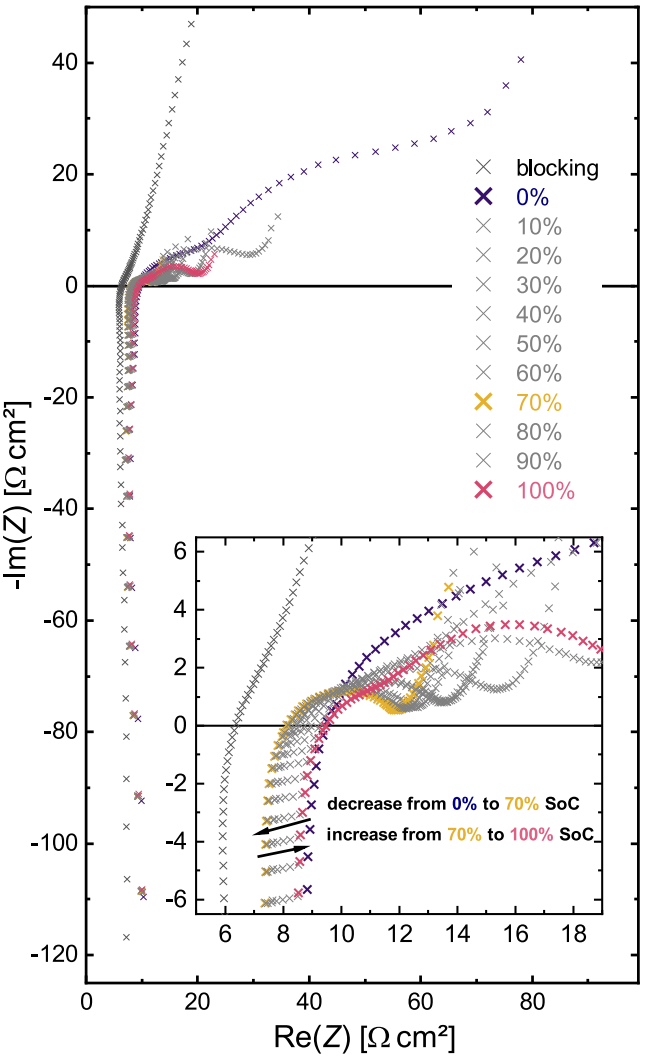


Figure A·2. Zoomed-out view of the Nyquist plots (from 100 kHz to 0.1 Hz) of the SoC-dependent cell impedance spectra of the 5.5 Ah Si||NCA MLP-cell after/formation/stabilization that are shown in Fig. 4a (normalized to the electrode area of 1475 cm^2). Note that the blocking spectrum corresponds to that shown in Fig. 3a. The inset is a zoomed-in view of the high-frequency region.

Effect of Cell Compression on the Cathode-Side Contact Resistance.—Figure A·3 shows Nyquist plots of MLP-cells from a single production batch, considered nominally identical, at 50% SoC after formation/stabilization under different cell compression levels. At the standard compression of 0.2 MPa that has been used throughout this study, neither the as-measured spectrum (black crosses; same spectrum as that shown in red in Fig. 4a) nor the

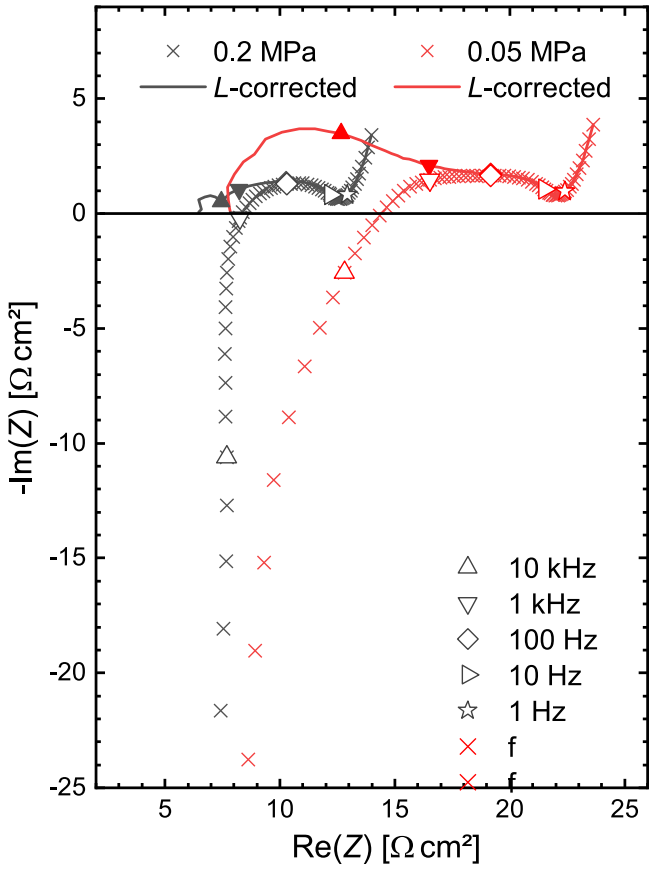


Figure A·3. Nyquist plots of the as-measured impedance response of nominal identical 5.5 Ah Si||NCA MLP-cells at 50% SoC (after formation/stabilization) under different clamping pressures, either at 0.2 MPa (black crosses; same spectrum as that shown in red in Fig. 4a or at 0.05 MPa (red crosses), shown between 50 kHz-0.1 Hz. The black and red solid lines show the corresponding *L*-corrected spectra.

L-corrected spectrum obtained from the high-frequency $L + R_{hf}^{*}$ ECM fit between 500–350 kHz ($L_\alpha = 0.14\ \mu H\ s^{(\alpha_L-1)}$, $\alpha_L = 0.99$; black solid line in Fig. A·3) reveal a distinct R_{cont}-related semi-circle. On the other hand, reducing the cell compression by a factor of four to 0.05 MPa (red crosses) shifts the apparent high-frequency resistance (–Im(Z) = 0 intercept) to higher Re(Z) values ($R_{hf,app} = 7.5\ \Omega\ cm^2$ at 0.2 MPa versus $14.1\ \Omega\ cm^2$ at 0.05 MPa). The associated *L*-corrected spectrum (red solid line), obtained by fitting the $L + R_{hf}^{*}$ ECM between 200–100 kHz (here limited to 200 kHz), with $L_\alpha = 0.11\ \mu H\ s^{(\alpha_L-1)}$ and $\alpha_L = 0.98$, reveals a clearly pronounced smeared-out semi-circle that can be attributed to the cathode-side R_{cont}. This demonstrates that the contact resistance must exceed a certain threshold to be resolved by the simplified *L*-subtraction procedure. Quantitatively, using the TLM-based ECM in Fig. 7b and the there described fitting approach, R_{cont} is found to increase ~5-fold when the cell compression is reduced from 0.2 MPa ($R_{cont} = 2.10 \pm 0.25\ \Omega\ cm^2$, Fig. 6e) to 0.05 MPa ($R_{cont} = 10.40 \pm 0.37\ \Omega\ cm^2$). A more detailed analysis of the pressure dependent evolution of R_{cont} during the MLP-cell aging is reported elsewhere.[32]

Electrolyte Composition of Pristine and End-of-Life MLP-Cells.—Figure A·4 shows the concentrations of the individual electrolyte components, i.e., of the $LiPF_6$ salt and of the FEC and DEC solvents, determined from extracted electrolyte samples from a pristine cell prior to formation as well as from an end-of-life cell (EoL at 70% SoH, reached at cycle 361; described in the context of

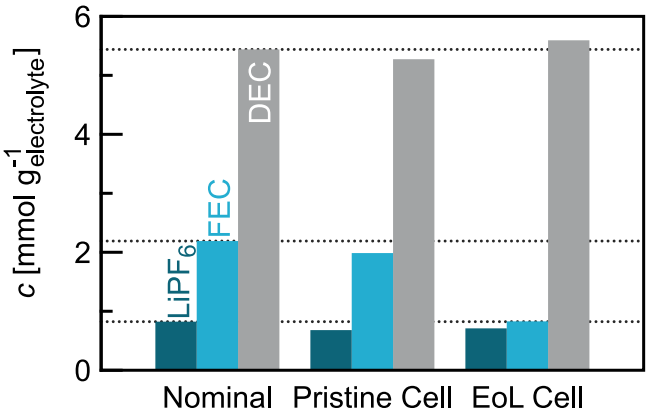


Figure A·4. Concentrations of the electrolyte components $LiPF_6$, FEC, and DEC determined via electrolyte extraction from a pristine cell prior to formation (middle set of bars) and of an end of life (EoL) cell, as described in the context of Fig. 8 (right set of bars). The horizontal dotted lines and left set of bars represent the nominal electrolyte component concentrations in as-received 1 M $LiPF_6$ in FEC:DEC 1:4 (v:v) electrolyte, assuming a density of 1.41 g cm^{-3} for FEC and a density of 0.975 g cm^{-3} for DEC. The concentrations were determined using the integral difference between the electrolyte species and the internal standard in ^{1}H-NMR and ^{19}F-NMR spectra.

Fig. 8). For comparison, the first set of bars and the corresponding horizontal dotted lines represent the nominal electrolyte component concentrations in fresh 1 M $LiPF_6$ in FEC:DEC 1:4 (v:v) electrolyte. Electrolyte samples were extracted and NMR measurements were performed as described in the experimental section. The EoL NMR data show that, within the error of the measurement, no $LiPF_6$ and no DEC but only FEC solvent was consumed, consistent with the findings for cells with silicon-based anodes and FEC-containing electrolyte.[56]

List of Symbols

Symbol	Description [unit]
A_{BET}	BET-specific surface area [$m^2\ g^{-1}$]
A_{geo}	Geometric electrode area [m^2]
α	Constant phase exponent [–]
C	C-rate for charging/discharging [–]
d	Diameter of wire [m]
f	Frequency [Hz]
f_{peak}	Peak Frequency, where the imaginary resistance attains its peak value [Hz]
j	Imaginary unit
L_α	Stray inductance [$H\ s^{(\alpha_L-1)}$]
l	Length of wire [m]
ω	Angular frequency (=$2\pi f$) [Rad/s]
Q_{cont}	Double layer capacitance at the electrode current collector interface [$F\ s^{(\alpha_{cont}-1)}$]
Q_{dl}	Double layer capacitance of an entire electrode [$F\ s^{(\alpha_{dl}-1)}$]
R_{cont}	Electrical contact resistance [Ω]
$R_{ct,an}$	Charge transfer resistance of an entire anode electrode [Ω]
$R_{ct,ca}$	Charge transfer resistance of an entire cathode electrode [Ω]
R_{el}	Electric resistance of the cell [Ω]
R_{hf}	High frequency resistance comprising R_{sep} and R_{el} [Ω]
$R_{hf,app}$	*Apparent* high-frequency resistance (*x*-axis intercept) [Ω]
R_{hf}^{*}	Estimated high-frequency resistance (from HF fit $L + R_{hf}^{*}$) [Ω]
R_{ion}	Ionic resistance within the electrode(= $d/(A\kappa_{eff})$) [Ω]
R_{sep}	Ionic resistance within the separator [Ω]
Z_L	Inductive impedance [Ω]
Z_{wb}	Warburg diffusion impedance [Ω]

ORCID

Simon Helmer https://orcid.org/0009-0006-0334-3297
Robert Morasch https://orcid.org/0000-0002-9931-1022
Philip Rapp https://orcid.org/0000-0001-7820-8117
Sven Friedrich https://orcid.org/0000-0003-1772-8076
Andreas Jossen https://orcid.org/0000-0003-0964-1405
Hubert A. Gasteiger https://orcid.org/0000-0001-8199-8703

References

1. L. Deleebeeck and S. Veltzé, "Electrochemical impedance spectroscopy study of commercial Li-ion phosphate batteries: A metrology perspective." *Int. J. Energy Res.*, **44**, 7158 (2020).
2. C. Lyu, T. Zhang, W. Luo, G. Wei, B. Ma, and L. Wang, "SOH Estimation of lithium-ion batteries based on fast time domain impedance spectroscopy." *Proceedings of the 14th IEEE Conference on Industrial Electronics and Applications, ICIEA 2019* (IEEE) 2142 (2019).
3. X. Wang, X. Wei, and H. Dai, "Estimation of state of health of lithium-ion batteries based on charge transfer resistance considering different temperature and state of charge." *J. Energy Storage*, **21**, 618 (2019).
4. H. S. Chan et al., "Comparison of methodologies to estimate state-of-health of commercial Li-ion cells from electrochemical frequency response data." *J. Power Sources J.*, **542**, 231814 (2022).
5. N. Meddings et al., "Application of electrochemical impedance spectroscopy to commercial Li-ion cells: A review." *J. Power Sources*, **480**, 228742 (2020).
6. K. M. Carthy, H. Gullapalli, K. M. Ryan, and T. Kennedy, "Review—Use of impedance spectroscopy for the estimation of Li-ion battery state of charge, state of health and internal temperature." *J. Electrochem. Soc.*, **168**, 080517 (2021).
7. X. Wang, X. Wei, J. Zhu, H. Dai, Y. Zheng, X. Xu, and Q. Chen, "A review of modeling, acquisition, and application of lithium-ion battery impedance for onboard battery management." *eTransportation*, **7**, 100093 (2021).
8. F. J. Günter, J. Keilhofer, V. Böhm, R. Daub, and G. Reinhart, "Wetting and inductivity in the impedance behavior of large lithium-ion cells." *J. Electrochem. Soc.*, **169**, 050522 (2022).
9. T. F. Landinger, G. Schwarzberger, and A. Jossen, "High frequency impedance characteristics of cylindrical lithium-ion cells: Physical-based modeling of cell state and cell design dependencies." *J. Power Sources*, **488**, 229463 (2021).
10. T. Momma, M. Matsunaga, D. Mukoyama, and T. Osaka, "Ac impedance analysis of lithium ion battery under temperature control." *J. Power Sources*, **216**, 304 (2012).
11. S. M. M. Alavi, C. R. Birkl, and D. A. Howey, "Time-domain fitting of battery electrochemical impedance models." *J. Power Sources*, **288**, 345 (2015).
12. T. Stanciu, D. I. Stroe, R. Teodorescu, and M. Swierczynski, "Extensive EIS characterization of commercially available lithium polymer battery cell for performance modelling." *17th European Conference on Power Electronics and Applications, EPE-ECCE Europe* (2015).
13. P. Kollmeyer, A. Hackl, and A. Emadi, "Li-ion battery model performance for automotive drive cycles with current pulse and EIS parameterization." *2017 IEEE Transportation and Electrification Conference and Expo, ITEC*486 (2017).
14. Y. Xie, J. Kim, M. Lee, J. Park, and W. Na, "An impedance behavior study of commercial NCA cylindrical battery cells at different SOCs." *J. Electrochem. Soc.*, **168**, 090548 (2021).
15. J. Landesfeind, D. Pritzl, and H. A. Gasteiger, "An analysis protocol for three-electrode Li-ion battery impedance spectra: Part I. Analysis of a high-voltage positive electrode." *J. Electrochem. Soc.*, **164**, A1773 (2017).
16. D. Pritzl, J. Landesfeind, S. Solchenbach, and H. A. Gasteiger, "An analysis protocol for three-electrode Li-ion battery impedance spectra: part II. Analysis of a graphite anode cycled versus LNMO." *J. Electrochem. Soc.*, **165**, A2145 (2018).
17. C. Berg, R. Morasch, M. Graf, and H. A. Gasteiger, "Comparison of silicon and graphite anodes: Temperature-dependence of impedance characteristics and rate performance." *J. Electrochem. Soc.*, **170**, 030534 (2023).
18. S. Solchenbach, D. Pritzl, E. J. Y. Kong, J. Landesfeind, and H. A. Gasteiger, "A gold micro-reference electrode for impedance and potential measurements in lithium ion batteries." *J. Electrochem. Soc.*, **163**, A2265 (2016).
19. J. Moškon and M. Gaberšček, "Transmission line models for evaluation of impedance response of insertion battery electrodes and cells." *J. Power Sources Adv.*, **7**, 100047 (2021).
20. R. Morasch, J. Keilhofer, H. A. Gasteiger, and B. Suthar, "Methods—Understanding porous electrode impedance and the implications for the impedance analysis of Li-ion battery electrodes." *J. Electrochem. Soc.*, **168**, 080519 (2021).
21. J. L. S. Dickmanns, L. Reuter, R. Morasch, F. Maglia, R. Jung, and H. A. Gasteiger, "Changes in structure and ionic resistance of lithium-ion battery graphite electrodes: Part I. Impact of formation and SEI." *J. Electrochem. Soc.*, **172**, 070513 (2025).
22. M. Gaberšček, J. Moskon, B. Erjavec, R. Dominko, and J. Jamnik, "The importance of interphase contacts in Li ion electrodes: The meaning of the high-frequency impedance arc." *Electrochem. Solid-State Lett.*, **11**, 170 (2008).
23. D. Pritzl, A. E. Bumberger, M. Wetjen, J. Landesfeind, S. Solchenbach, and H. A. Gasteiger, "Identifying contact resistances in high-voltage cathodes by impedance spectroscopy." *J. Electrochem. Soc.*, **166**, A582 (2019).
24. S. Schindler and M. A. Danzer, "Influence of cell design on impedance characteristics of cylindrical lithium-ion cells: A model-based assessment from electrode to cell level." *J. Energy Storage*, **12**, 157 (2017).
25. BioLogic, (2023), Biologic, Application Note - Precautions for good impedance measurements, https://www.biologic.net/documents/eis-precautions-electrochemistry-battery-application-note-5/.
26. P. Korth Pereira Ferraz, R. Schmidt, D. Kober, and J. Kowal, "A high frequency model for predicting the behavior of lithium-ion batteries connected to fast switching power electronics." *J. Energy Storage*, **18**, 40 (2018).
27. F. F. Oehler, A. Graule, S. Kücher, T. Roth, A. Adam, J. Li, E. Ronge, R. Mörtel, and A. Jossen, "Multi-reference electrode lithium-ion pouch cell design for spatially resolved half-cell potential and impedance measurements." *J. Electrochem. Soc.*, **170**, 110522 (2023).
28. E. B. Rosa and F. W. Grover, "Formulas and tables for the calculation of mutual and self-inductance." *Bulletin of the Bureau of Standards*, **8**, p. 150 (1912), Courier Corporation.
29. J. Landesfeind, J. Hattendorff, A. Ehrl, W. A. Wall, and H. A. Gasteiger, "Tortuosity determination of battery electrodes and separators by impedance spectroscopy." *J. Electrochem. Soc.*, **163**, A1373 (2016).
30. D. Schreiner et al., "Comparative evaluation of LMR-NCM and NCA cathode active materials in multilayer lithium-ion pouch cells: Part I. Production, electrode characterization, and formation." *J. Electrochem. Soc.*, **168**, 030507 (2021).
31. S. Friedrich, S. Stojcevic, P. Rapp, S. Helmer, M. Bock, A. Durdel, H. A. Gasteiger, and A. Jossen, "Effect of mechanical pressure on lifetime, expansion, and porosity of silicon-dominant anodes in laboratory lithium-ion cells." *J. Electrochem. Soc.*, **171**, 050540 (2024).
32. S. Friedrich, S. Helmer, L. Reuter, J. L. S. Dickmanns, A. Durdel, and A. Jossen, "Effect of mechanical pressure on rate capability, lifetime, and expansion in multilayer pouch cells with silicon-dominant anodes." *J. Electrochem. Soc.*, **171**, 090503 (2024).
33. Y. Hoshi, Y. Narita, K. Honda, T. Ohtaki, I. Shitanda, and M. Itagaki, "Optimization of reference electrode position in a three-electrode cell for impedance measurements in lithium-ion rechargeable battery by finite element method." *J. Power Sources*, **288**, 168 (2015).
34. H. Nara, D. Mukoyama, T. Yokoshima, T. Momma, and T. Osaka, "Impedance analysis with transmission line model for reaction distribution in a pouch type lithium-ion battery by using micro reference electrode." *J. Electrochem. Soc.*, **163**, A434 (2016).
35. S. Yi, B. Wang, Z. Chen, R. Wang, and D. Wang, "A study on $LiFePO_4$/graphite cells with built-in $Li_4Ti_5O_{12}$ reference electrodes." *RSC Adv.*, **8**, 18597 (2018).
36. L. Hartmann, L. Reuter, L. Wallisch, A. Beiersdorfer, A. Adam, D. Goldbach, T. Teufl, P. Lamp, H. Gasteiger, and J. Wandt, "Depletion of electrolyte salt upon calendaric aging of lithium-ion batteries and its effect on cell performance." *J. Electrochem. Soc.*, **171**, 060506 (2024).
37. L. M. Thompson, J. E. Harlow, A. Eldesoky, M. K. G. Bauer, J. H. Cheng, W. S. Stone, T. Taskovic, C. R. M. McFarlane, and J. R. Dahn, "Study of electrolyte and electrode composition changes versus time in aged Li-ion cells." *J. Electrochem. Soc.*, **168**, 020532 (2021).
38. N. Ogihara, S. Kawauchi, C. Okuda, Y. Itou, Y. Takeuchi, and Y. Ukyo, "Theoretical and experimental analysis of porous electrodes for lithium-ion batteries by electrochemical impedance spectroscopy using a symmetric cell." *J. Electrochem. Soc.*, **159**, A1034 (2012).
39. H. Nara, D. Mukoyama, R. Shimizu, T. Momma, and T. Osaka, "Systematic analysis of interfacial resistance between the cathode layer and the current collector in lithium-ion batteries by electrochemical impedance spectroscopy." *J. Power Sources*, **409**, 139 (2019).
40. C. Busson, M. Blin, P. Guichard, P. Soudan, O. Crosnier, D. Guyomard, and B. Lestriez, "A primed current collector for high performance carbon-coated $LiFePO_4$ electrodes with no carbon additive." *J. Power Sources*, **406**, 7 (2018).
41. I. V. Thorat, D. E. Stephenson, N. A. Zacharias, K. Zaghib, J. N. Harb, and D. R. Wheeler, "Quantifying tortuosity in porous Li-ion battery materials." *J. Power Sources*, **188**, 592 (2009).
42. S. Grabmann, L. Mayr, M. K. Kick, and M. F. Zaeh, "Enhancing laser-based contacting of aluminum current collector foils for the production of lithium-ion batteries using a nanosecond pulsed fiber laser." *Procedia CIRP*, **111**, 778 (2022), Elsevier B.V.
43. H. S. Shin and M. de Leon, "Mechanical performance and electrical resistance of ultrasonic welded multiple Cu-Al layers." *J. Mater. Process. Technol.*, **241**, 141 (2017).
44. C. M. Berg, R. Morasch, and H. A. Gasteiger, "Silicon hysteresis and voltage relaxation phenomena: Implications on the characterization of anode overpotentials." *J. Electrochem. Soc.*, **172**, 050516 (2025).
45. S. Helmer, J. L. S. Dickmanns, R. Wilhelm, and H. A. Gasteiger, "Unraveling the influence of the electrical resistance in porous microscale silicon electrodes employing impedance spectroscopy." *Manuscr. Prep.*
46. D. Jantke, R. Bernhard, E. Hanelt, T. Buhrmester, J. Pfeiffer, and S. Haufe, "Silicon-dominant anodes based on microscale silicon particles under partial lithiation with high capacity and cycle stability." *J. Electrochem. Soc.*, **166**, A3881 (2019).
47. M. Graf, C. Berg, R. Bernhard, S. Haufe, J. Pfeiffer, and H. A. Gasteiger, "Effect and progress of the amorphization process for microscale silicon particles under partial lithiation as active material in lithium-ion batteries." *J. Electrochem. Soc.*, **169**, 020536 (2022).
48. S. Haufe, R. Bernhard, and J. Pfeiffer, "Revealing the failure mechanism of partially lithiated silicon-dominant anodes based on microscale silicon particles." *J. Electrochem. Soc.*, **168**, 080531 (2021).
49. F. Paloukis, C. Elmasides, F. Farmakis, P. Selinis, S. G. Neophytides, and N. Georgoulas, "Electrochemical impedance spectroscopy study in micro-grain structured amorphous silicon anodes for lithium-ion batteries." *J. Power Sources*, **331**, 285 (2016).

50. Y. Ko, C. Hwang, and H. K. Song, "Investigation on silicon alloying kinetics during lithiation by galvanostatic impedance spectroscopy." *J. Power Sources*, **315**, 145 (2016).
51. F. Friedrich, B. Strehle, A. T. S. Freiberg, K. Kleiner, S. J. Day, C. Erk, M. Piana, and H. A. Gasteiger, "Editors' Choice—Capacity fading mechanisms of NCM-811 cathodes in lithium-ion batteries studied by X-ray diffraction and other diagnostics." *J. Electrochem. Soc.*, **166**, A3760 (2019).
52. T. Teufl, D. Pritzl, S. Solchenbach, H. A. Gasteiger, and M. A. Mendez, "Editors' Choice—State of charge dependent resistance build-up in Li- and Mn-rich layered oxides during lithium extraction and insertion." *J. Electrochem. Soc.*, **166**, A1275 (2019).
53. T. Ma et al., "Revisiting the corrosion of the aluminum current collector in lithium-ion batteries." *J. Phys. Chem. Lett.*, **8**, 1072 (2017).
54. R. Amin, D. B. Ravnsbæk, and Y.-M. Chiang, "Characterization of electronic and ionic transport in $Li_{1-x}Ni_{0.8}Co_{0.15}Al_{0.05}O_2$ (NCA)." *J. Electrochem. Soc.*, **162**, A1163 (2015).
55. F. B. Spingler, S. Kücher, R. Phillips, E. Moyassari, and A. Jossen, "Electrochemically stable in situ dilatometry of NMC, NCA and graphite electrodes for lithium-ion cells compared to XRD measurements." *J. Electrochem. Soc.*, **168**, 040515 (2021).
56. R. Jung, M. Metzger, D. Haering, S. Solchenbach, C. Marino, N. Tsiouvaras, C. Stinner, and H. A. Gasteiger, "Consumption of fluoroethylene carbonate (FEC) on Si-C composite electrodes for Li-ion batteries." *J. Electrochem. Soc.*, **163**, A1705 (2016).